國立交通大學

光電工程研究所

碩士論文

向列型液晶 E7 在不同溫度下的光學常數之時析兆赫光譜研究

Terahertz Time-Domain Spectroscopic Studies of the Temperature-Dependent Optical Constants of the Eutectic Liquid Crystal E7

研 究 生：楊承山

指導教授：潘犀靈　教授

中 華 民 國 九 十 八 年 六 月

向列型液晶 E7 在不同溫度下的光學常數之時析兆赫光譜研究

Terahertz Time-Domain Spectroscopic Studies of the Temperature-Dependent Optical Constants of the Eutectic Liquid Crystal E7

研究生：**楊承山**　　Student：**Chan-Shan Yang**

指導教授：**潘犀靈**　教授　　Advisor：**Prof. Ci-Ling Pan**

國 立 交 通 大 學

光電工程研究所

碩 士 論 文

A Thesis

Submitted to Institute of Electro-Optical Engineering

College of Electrical Engineering and Computer Science

National Chiao Tung University

In Partial Fulfillment of the Requirements

For the Degree of

Master of Engineering

In Electro-Optical Engineering

June 2009

Hsinchu, Taiwan, Republic of China

中華民國九十八年六月

向列型液晶 E7 在不同溫度下的光學常數之時析兆赫光譜研究

研究生：楊承山　　指導教授：潘犀靈 教授

國立交通大學光電工程研究所

摘 要

兆赫波時域光譜技術是一種研究物質在兆赫波段光學性質的方法。本論文是利用兆赫波時域光譜技術來研究一種已經被廣泛運用在可見光波段的混合性向列型液晶 E7，其在向列相和均相態時，在不同溫度(從攝氏 26 度至攝氏 70 度)以及**頻率範圍**(0.2 THz ~ 1.4 THz)的光學常數。實驗結果顯示此種液晶在兆赫波段下仍保有正的複折射現象，而且**複數折射率的虛數部分皆小於** 0.04，也沒有明顯的吸收譜線。在攝氏 26 度時，**E7 的長軸方向與短軸方向折射率分別約為** 1.71 **與** 1.57，即其**雙折射約為** 0.14。另外，我們從雙折射數據中所得到的**液晶有序參數資訊也與可見光波段者吻合**，由此更確定了此次量測的準確性。另一方面，本研究也成功地驗證液晶**折射率溫度相依的 extended Cauchy equations**。本研究成果也將會是液晶元件日後在遠紅外區波段各種應用的重要依據。

Terahertz Time-Domain Spectroscopic Studies of the Temperature-Dependent Optical Constants of the Eutectic Liquid Crystal E7

Student: Chan-Shan Yang Advisor: Prof. Ci-Ling Pan

Institute of Electro-Optical Engineering
College of Electrical Engineering and Computer Science
National Chiao Tung University

Abstract

We have used terahertz (THz) time-domain spectroscopy to investigate the frequency dependence and temperature dependence of the optical constants of a widely used liquid crystal mixture E7 in both nematic and isotropic phases. The extinction coefficient of E7 at room temperature is less than 0.04 and without sharp absorption features in the frequency range of 0.2~1.4 THz. The extraordinary and ordinary indices of refraction at 26°C are around 1.71 and 1.57, respectively, giving rise to a birefringence of about 0.14 in this frequency range. The temperature-dependent order parameter extracted from birefringence data agrees with values in the visible region quite well. On the other hand, the extended Cauchy equations describing the temperature dependence of refractive indices of liquid crystal is also confirmed in this study.

Acknowledgements

轉瞬間，時間已是 2009 年的暑日。想起五年前剛進來光電這個大家庭的青澀模樣，我不禁想要跟所有幫助過我的人、指導我的人和關愛我的人說一聲「謝謝」。也許這對某些人只是兩個很簡單的音節，但對我來說，卻灌注了五年中所有的記憶與感動。

其中最要感謝的，就是我從大一到碩士班的指導老師**潘犀靈 教授**以及在實驗上給我諸多意見與幫助的**趙如蘋 教授**。如果沒有他們費心的指導，細心的提醒以及耐心的包容，我想這一本碩士論文定無法如此順利的完成。除此之外，課餘間在老師家的師生活動與私下的關心談話，也因為知道後面一定會有老師的支撐和諒解，進而也構築了我對研究的信心與熱情。

除此之外，實驗室的學長姐 **宇泰**、**怡超**、**晉瑋**、**宜貞**、**卓帆**和**家任**，總在我最徬徨無助時，給予我最誠懇且受用的建議。在比較熟悉的宇泰、怡超和晉瑋學長身上，我更看到了一位”能者”所應有的風範與態度，一種我會想要追隨的態度。

我的同學們，**晏徵**、**俞良**、**阿猛**和**阿駿**，能與你們身處在同一間實驗室並且一同修課，是我非常難忘記的經歷和感受。你們的優秀，讓我自省本身的不足；你們的真誠，讓我們相處的方式能夠輕鬆泰然；你們的執著，讓我學會不再輕言放棄。相信在很久的以後，你們都能找到自己的夢想，自傲的各立一方。而剛認識的**睿茵**、**聖司**和**冠儒**，也謝謝你們在畢業季節的時候，對實驗室多番的幫忙及貢獻，更希望你們對日後的研究都能一帆風順並充滿熱情。

最後，我要對在背後支撐我的**父親**、**母親**、**弟弟**、**叔叔**、**嬸嬸**和**宜珊**說一聲”謝謝”。謝謝你們一直以來的的照顧與包容，若沒有這些元素，我相信自己在求學的路途上，無法如此的勇敢和堅毅。特別是父親與母親，你們給的是我生命價值中最重要的一部分，我會用一輩子的時間來證明它。

我是一幅周圍有殘缺的拼圖，曾經我很膚淺的只看到中間完整的部分，但是因為你們，我慢慢看到並找回不足的地方。也許需要一點時間，不過我知道自己真的在改變。謝謝~~

Chan-Shan Yang

2009.07　風城~交大

Table of Contents

中文摘要 i
Abstract ii
Acknowledgements iii
Table of Contents iv
List of Figures vi
List of Tables ix
Chapter 1 Introduction 1
1.1 What is Terahertz (THz) 1
1.2 Liquid Crystals (LCs) 3
1.2-1 Thermotropic LCs 3
1.2-2 Mixtures 4
1.2-3 Nematic Liquid Crystal (NLC) 5
1.3 THz Liquid Crystals Optics 8
1.4 Thesis Highlight 9
Chapter 2 Experimental Methods 10
2.1 The Preparation of LC Cell and Reference Cell 10
2.2 Temperature and Humidity Controlled System 16
2.3 THz Time-domain Spectroscopy (THz-TDS) 19
2.3-1 Introduction 19
2.3-2 Theory of Generating THz Radiation 20
2.3-2-1 Optical Rectification 21
2.3-2-2 Photoconductive(PC) Switch 22
2.3-2-3 Current-Surge Model 23
2.3-2-4 Drude-Lorentz model 28
2.3-3 Theory of Detecting THz Radiation 30
2.3-4 Antenna-based Emitter and Detector 31
2.3-5 THz-TDS with Collimated Beam System 33
Chapter 3 Extraction of Optical Constants from THz Time-domain Spectroscopic Measurements 35
3.1 Introduction 35
3.2 Determination of Optical Constants 38
3.3 A Model Describing the Temperature Effect of LC Refractive Indices 41
3.3-1 Effective Medium Theory 41
3.3-1-1 Depolarization Field 41
3.3-1-2 Local Electric Field of Single Atom 42
3.3-1-3 Lorentz Field 43

3.3-1-4 Dielectric Constant and Polarizability 44
3.3-2 Extended Cauchy Equations 45
Chapter 4 Results and Discussions 49
4.1 Complex Optical Constants 49
4.2 Temperature Dependence of Refractive Indices 54
4.2-1 Temperature Effect on Real Refractive Indices 54
4.2-2 Temperature Effect on $< n^2 >$ and $< n >$ 59
4.3 Temperature Effect on Birefringence and Order Parameter 67
4.4 Temperature Dependence of Gradient of Refractive Indices 72
Chapter 5 Conclusions 75
References 76

List of Figures

Fig. 1.1	The diagram shows the name and the applications in different frequency ranges.	2
Fig. 1.2	Molecular alignments of LCs.	4
Fig. 1.3	Molecular structures of the four elements making up the LC E7.	5
Fig. 1.4	The three types of deformation occurring in nematics.	6
Fig. 1.5	The angle between the director of LC molecules and the propagation direction of incident light.	8
Fig. 2.1	Sketches of (a) LC cell and (b) the reference cell.	10
Fig. 2.2	The procedure of preparing the LC cell.	11
Fig. 2.3	The conversion of the original coordinate (x, y) and the new coordinate ($x^{'}, y^{'}$).	13
Fig. 2.4	The pictures of the temperature-controlled sample holder.	16
Fig. 2.5	The pictures of the temperature controller and the probe.	17
Fig. 2.6	The testing result which is set at $26^{o}C$ of the temperature control system.	17
Fig. 2.7(a)	Temporal profiles of THz before and after purging.	18
Fig. 2.7(b)	Frequency domain of THz before and after purging.	19
Fig. 2.8	The general setup of the antenna-based time domain spectroscopy system.	20
Fig. 2.9	Optical rectification.	22
Fig. 2.10	Photoconductive switch.	23
Fig. 2.11	Schematic of the THz-TDS.	34
Fig. 3.1	The symbols of deriving the complex refractive index.	40
Fig. 3.2	The depolarization field E_P is opposite to P. The fictitious surface charges are indicate. The field of these charges is E_P within the ellipsoid.	42
Fig. 3.3	The internal electric field on an atom in a crystal is the sum of the external applied field $\vec{E}_0$ and of the field due to the other atoms in the crystal.	43
Fig. 3.4	Estimation of the field in a spherical fiction in a uniformly polarized medium.	44
Fig. 4.1	Transmitted THz signals (*e* ray) through the reference (solid line) and LC cell (dashed line) at 26°C for (a) e-ray and (b) o-ray.	49
Fig. 4.2	Power spectra. Oo the transmitted THz signals (*e* ray) through	50

	the reference (solid line) and LC cell (dashed line) at 26°C for (a) o-ray and (b) e-ray.	
Fig. 4.3	The real refractive indices of E7 are plotted as fuctions of frequency.	51
Fig. 4.4	The imaginary refractive indices of E7 are plotted as functions of frequency.	52
Fig. 4.5(a)	The real refractive indices of fused silica are plotted as fuctions of frequency at 26°C.	53
Fig. 4.5(b)	The imaginary refractive indices of E7 are plotted as functions of frequency at 26°C.	53
Fig. 4.6(a)	Extraodinary and ordinary refractive indices of E7 are plotted as functions of reduced temperature at frequency of 0.34, 0.41, 0.53, 0.70, 0.80 and 0.90 THz.	56
Fig. 4.6(b)	Extraodinary and ordinary refractive indices of E7 are plotted as functions of reduced temperature at frequency of 0.98, 1.10, 1.19, 1.29 and 1.40 THz.	57
Fig. 4.7	Extraodinary and ordinary refractive indices of E7 are plotted as functions of reduced temperature at frequency of 0.34 (Black), 0.70 (Red) and 0.98 (Blue) THz.	58
Fig. 4.8(a)	Average refractive indices of E7 are plotted as functions of reduced temperature at frequency of 0.34, 0.41, 0.53, 0.70, 0.80 and 0.90 THz.	60
Fig. 4.8(b)	Average refractive indices of E7 are plotted as functions of reduced temperature at frequency of 0.98, 1.10, 1.19, 1.29 and 1.40 THz.	61
Fig. 4.9	Average refractive indices of E7 are plotted as functions of reduced temperature at frequency of 0.70 (**Black**), 0.89 (**Red**), 1.10 (**Green**), and 1.40 (**Blue**) THz.	62
Fig. 4.10(a)	$<n^2>$ of E7 are plotted as functions of reduced temperature at frequency of 0.34, 0.41, 0.53, 0.70, 0.80 and 0.90 THz.	64
Fig. 4.10(b)	$<n^2>$ of E7 are plotted as functions of reduced temperature at frequency of 0.98, 1.10, 1.19, 1.29 and 1.40 THz.	65
Fig. 4.11	$<n^2>$ of E7 are plotted as functions of reduced temperature at frequency of 0.70 (**Black**), 0.89 (**Red**), 1.10 (**Green**), and 1.40 (**Blue**) THz.	67
Fig. 4.12(a)	Δn of E7 are plotted as functions of reduced temperature at frequency of 0.34, 0.41, 0.53, 0.709, 0.80 and 0.90 THz.	69
Fig. 4.12(b)	Δn of E7 are plotted as functions of reduced temperature at	70

frequency of 0.98, 1.10, 1.19, 1.30 and 1.40 THz.

Fig. 4.13 Birefringence of E7 are plotted as functions of reduced temperature at frequency of 0.34 (**Black**), 0.80 (**Red**) and 1.10 (**Blue**) THz. 71

Fig. 4.14 Birefringence of E7 measured at 26°C are plotted as a function of frequency. 72

Fig. 4.15 Temperature-dependent $\frac{dn_e}{dT}$ of E7 at different frequencies (0.34, 0.41, 0.53, 0.70, 0.80, 0.89, 0.98, 1.10, 1.19, 1.29 and 1.40 THz), respectively. 73

Fig. 4.16 Temperature-dependent $\frac{dn_o}{dT}$ of E7 at different frequencies (0.34, 0.41, 0.53, 0.70, 0.80, 0.89, 0.98, 1.10, 1.19, 1.29 and 1.40 THz), respectively. 74

Fig. 4.17 Temperature-dependent $\frac{dn_o}{dT}$ of E7 at 0.41(THz). 74

List of Tables

Table. 3.1	The references measuring optical constants of E7 in different frequency range.	36
Table. 4.1	The fitting parameters of Eq. (3.33) and (3.34) for frequencies from 0.34 to 1.40 THz.	55
Table. 4.2	The fitting parameters of Eq. (3.31) for frequencies from 0.34 to 1.40THz.	59
Table. 4.3	The fitting parameters of Eq. (3.37) for frequencies from 0.34 to 1.40THz.	66
Table. 4.4	The fitting parameters of Eq. (3.38) for frequencies from 0.34 to 1.40THz.	68

Chapter 1 Introduction

The large birefringence of liquid crystals (LCs) well known can be easily controlled by electric or magnetic field. According to the distinguishing characteristic, application based on LCs have developed widely and rapidly, such as liquid crystal displays which have established a substantial foothold on the market as flat panel displays for computers, transportation, communication and, with increasing importance for TV in the future [**1**], as well as their extraordinary and ordinary refractive indices (n_e and n_o), are essential for the modulation of millimeter-wave, infrared, visible region. Among the application of them, phase shifters [**2**], attenuator, polarizers and wavelength selection filters [**3**] have been demonstrated. However, the applications and research of LCs should be extended to THz range because of the remarkable development of terahertz (THz) technology [**4**]. For this purpose, we have to measure accurate refractive indices and the birefringence of LC is necessary for THz applications.

In writing this section, the basic information of THz technology, photoconductive (PC) antenna, THz time-domain-spectroscopy (THz-TDS) and nematic LCs (NLCs) are mentioned, and the structure of the thesis is presented in the last part of this chapter as "Thesis highlight".

1.1 What is Terahertz (THz)

The THz region of the electromagnetic spectrum where until recently bright sources of light and sensitive means of detection have not existed represents the wavelength range and frequency range between 300*μm*~*1000μm* and 100GHz~30THz as shown in **Fig. 1.1**, respectively [**4,5**]. On the other hand, this corresponds to wavelengths between 1*mm* and 0.03*mm*, so THz is also called sub-millimeter wave. The preceding extreme is located just on

the microwave region where satellite dishes and mobile phones operate, and the latter one lies adjacent to infrared region used in devices such as TV remote controllers. However, the efficient and reliable sources and detector of THz radiation are not available easily because not only the conventional microwave source can not work at high enough frequencies, but the thermal effect confines the laser diode sources. Therefore, the development of THz has been held back for a long time. This predicament becomes better in the recent years because of the technology of self-mode-locked operation in Ti:sapphire oscillators [**6**], there has been a great progress in the generation of ~100 fs pulses. Because the semiconductor irradiated by ultrafast pulses can generate the broadband THz radiation, van Exter et al. demonstrated a dipole antenna based on semiconductor in 1989 [**7**] and showed the system as a spectroscopy with off-axis paraboloidal mirrors [**8**]. In 1990, Zhang et al. developed the way of generating subpicosecond pulses from a semiconductor surface [**9**]. After that, the same author presented free-space electro-optic sampling technology to improve signal to noise ratio (S/N ratio) to 10^4 and to carry out much large dynamic range in 1996 [**10**]. Above of all, a spectroscopic technique using pulsed THz radiation has been accomplished and called "THz time-domain spectroscopy (THz-TDS)".

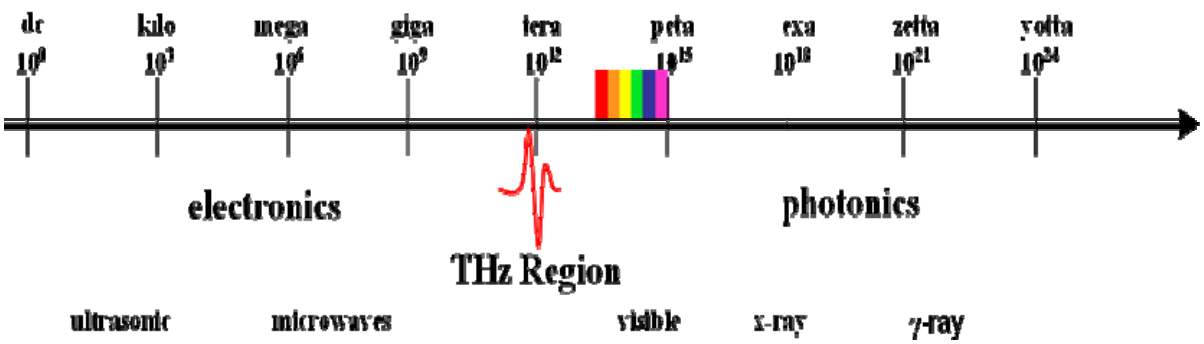

Figure 1.1 The diagram shows the name and the applications in different frequency ranges. The THz region lies between photonics and electronics regimes.
(Modification from X.-C.Zhang, published in 2005)

Much of the applications in THz radiation originate from penetrating deep into many organic materials without the damage. Besides, THz radiation is also absorbed by water easily, so that varying water content can discriminate the material from other ones. These characteristics lend themselves to applications in process and quality control as well as biomedical imaging, and some groups have presented THz imaging as a way of monitoring packages at airport. But for further advances in many applications, variety of active and passive THz optical elements are demanded, such as detectors, modulators, phase shifters and polarizers. Unfortunately, these devices in the region are investigated deficiently. Therefore, the development and research of THz optical devices are a burning issue.

1.2 Liquid Crystals (LCs)

1.2-1 Thermotropic LCs

Thermotropic LCs are extensively studied and used widely because of their linear as well as nonlinear optical characteristics. “Thermotropic” means that they exhibit different liquid crystalline phases as a function of temperature. Thermotropic LCs shown as **Figure 1.2** includes nematic phase, smectic phase, chiral phase. However, nematic phase is most common investigated; the LCs utilized in our work is all rod-like nematic LCs, where the molecules have no positional order, but they have long-range orientational order.

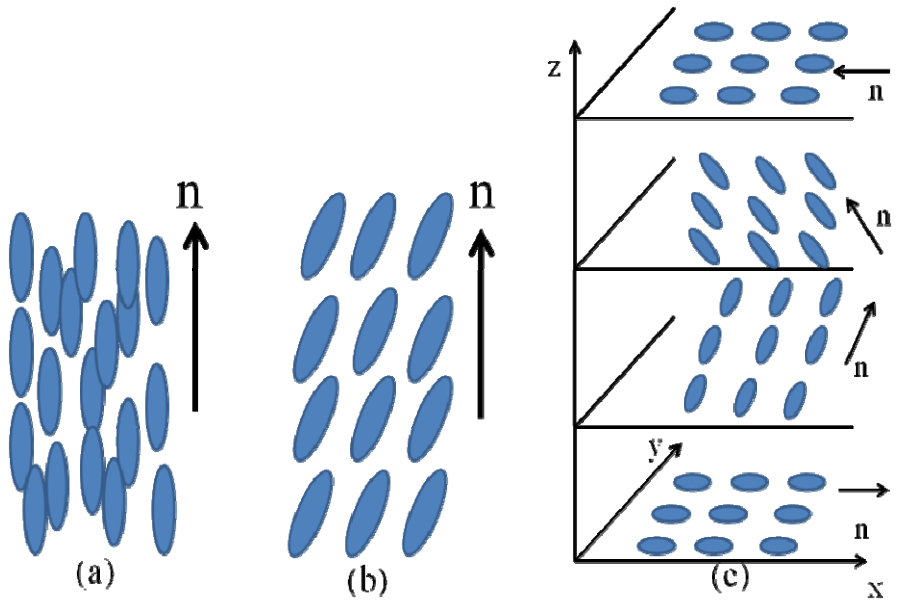

Figure 1.2 Molecular alignments of LCs: (a) Nematic; (b) Smectic-C; (c) Cholesteric

1.2-2 Mixtures

For pure LCs, temperature ranges for the various mesophases and other physical limitations makes lots of disadvantages imposed on application of these material [**11**]. In order to fixing these shortcomings, eutectic mixtures of two or more LCs are used widely. One of examples is E7 which being a mixture of four liquid crystals, and the molecular structures are shown as **Figure 1.3**. There are many different points between the individual mixture constituents and E7, such as dielectric anisotropics and optical constants et al.. After making the right mixture, the phase diagram will change, and the range between melting and clearing temperatures will be also larger than the individual constituents.

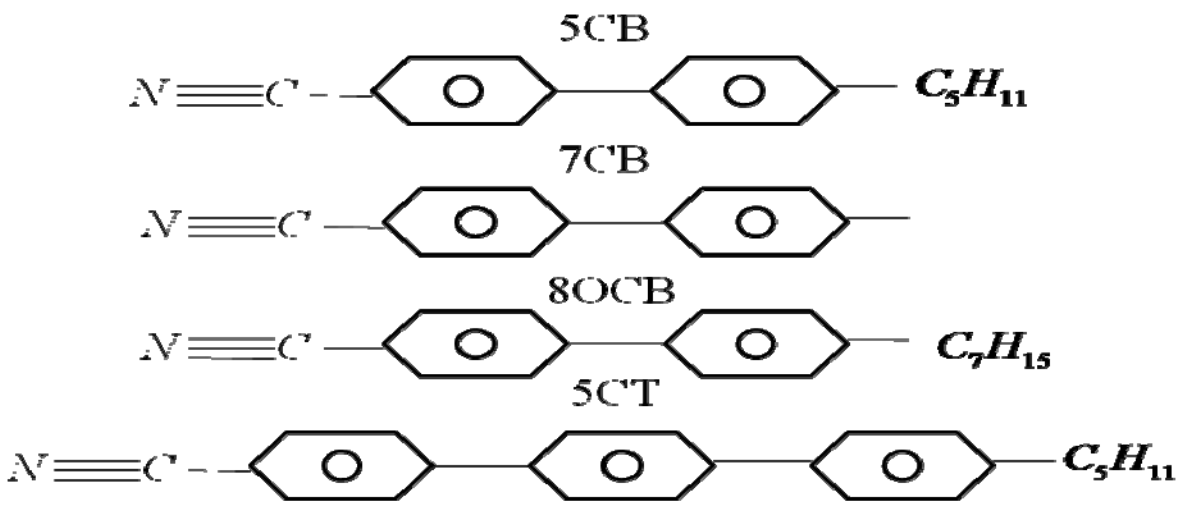

Figure 1.3 Molecular structures of the four elements making up the LC E7.

1.2-3 Nematic Liquid Crystal (NLC)

In general, the most common LC phase is the nematic phase. The LCs used in our works is also one of rod-like nematic LCs. The nematic ("thread" in Greek) LC has a high degree of long-range orientational order of the molecules. It differs from the isotropic liquid in that the molecules are spontaneously oriented with a common axis, labeled by a unit vector (or "director"). The states of the director $\hat{n}$ and $-\hat{n}$ are indistinguishable in nematic. The director usually varies from point to point in the medium, but a uniformly aligned sample is optically uniaxial with large birefringence. The rotational symmetry of the system can be broken by the particular boundary conditions (ex. Polyimide film, DMOAP coating…etc). The LC molecules around the particularly treated surface tend to orientate with some specific direction, which is the general method to align LCs [**12**].

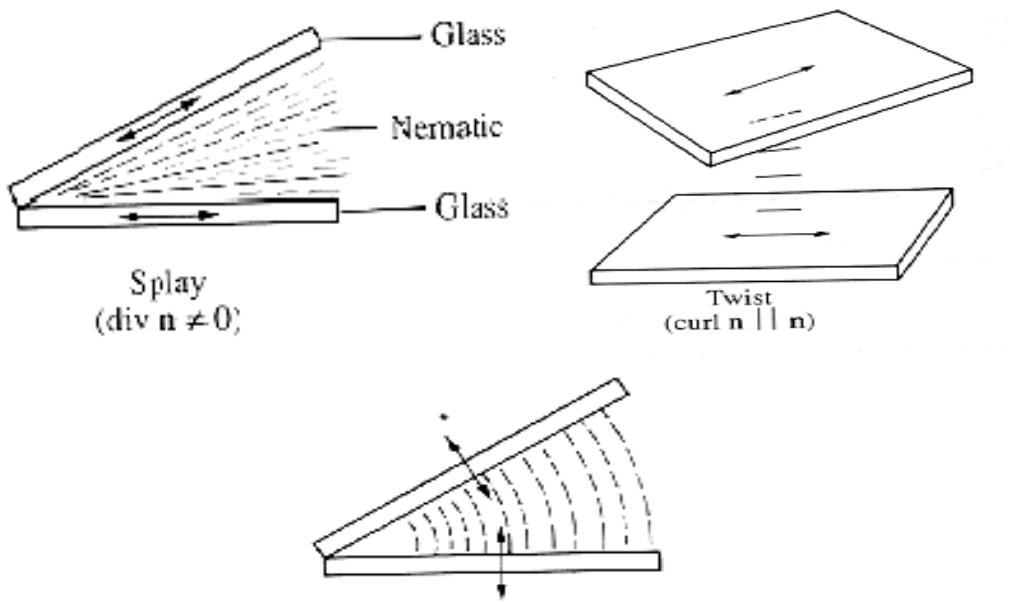

Figure 1.4 The three types of deformation occurring in nematics. The figure shows how each type may be obtained separately by suitable glass walls. (Reproduced from P. G. de Gennes and J. Prost, The Physics of Liquid Crystals, 2nd ed. , Oxford, New York, 1983)

If the LC molecules don't orientate parallel to each other, the total energy of the system increases and the deformation exists. Three typical types of the deformation (splay, twist and bend) occur in nematic phase shown in **Fig. 1.4**. The deformation (or distortion) comes from the perturbations of the boundary condition, external field, chiral dopant …etc. The external field, such as electric field or magnetic field, can be used to re-orientate the LC molecules. Briefly, the LC molecules tend to be parallel or perpendicular (mostly parallel) to the field and the extra energy density due to the field is the function of the direction and magnitude of the field. We now consider a strong boundary case, the LC molecules around the boundary will be aligned and some deformation exists in the bulk due to the configuration of the lowest total energy. If we put the external electric/magnetic field on it, the total energy, F, can be described as

$$F = \int (f_d + f_{E/M}) d\rho \,. \qquad \textbf{(1.1)}$$

Where the f_d and $f_{E/M}$ are the extra energy from the deformation and the external electric/magnetic field and ρ is the unit volume. For the parallel case (the LC molecules tend to orientate with the field direction), when the molecules orientate closer to the field direction, the f_d increases and the $f_{E/M}$ decreases. The molecules will be aligned again with the request of the lowest total energy for the stable state. In other words, the deformation term dominates mainly with weak field and the field term dominates for strong field. According to the continuum theory, the director, $\hat{n}$, spatially varies slowly and smoothly and the system keeps the long-range order.

As we have mentioned, the LC molecules tend to be parallel to the director such that the aligned nematic forms an optically uniaxial system. The difference between refractive indices measured with polarization parallel or normal to $\hat{n}$ is quite large. The ordinary index n_o is for light with the polarization perpendicular to the director and the extraordinary refractive index n_e is for light with the polarization parallel to the director. The n_o and n_e of E7 in visible range are shown by Shin-Tson Wu [**13**]. The birefringence, or double refraction of the nematic, is defined as [**14**]

$$\Delta n = n_e - n_o . \tag{1.2}$$

When the incident polarization of light is not parallel to the director, the index of the refraction for the extraordinary ray should be written as

$$n_{eff} = \left(\frac{\sin^2\theta}{n_{//}^{\ 2}} + \frac{\cos^2\theta}{n_{\perp}^{\ 2}}\right)^{-1/2}, \tag{1.3}$$

where θ is the angle between the propagation direction of the incident light and the optical axis as shown in **Fig. 1.5**. Therefore, the effective birefringence is $\Delta n = n_{eff} - n_o$.

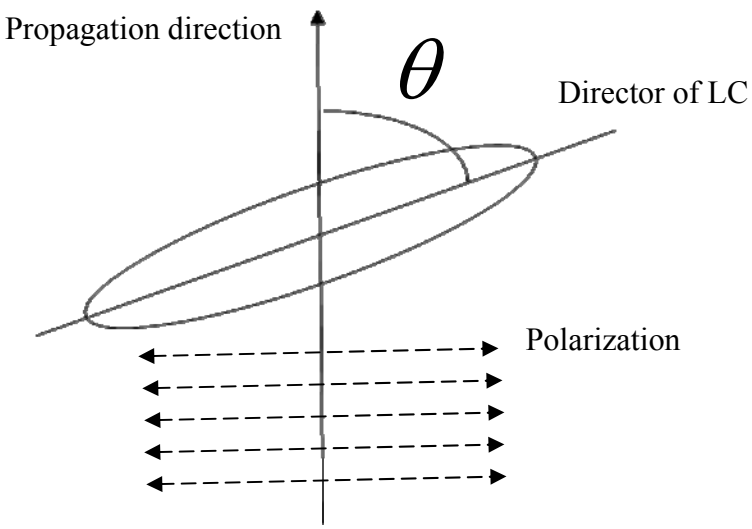

Figure 1.5 The angle, θ, between the director of LC molecules and the propagation direction of incident light will affect the effective index of extraordinary wave.

1.3 THz liquid crystals optics

Thanks to its relative large birefringence ($\Delta n = n_e - n_o$) from the visible to microwave band, liquid crystals (LCs), have found a varity of application ranging from display, communication and signal processing, beam steering, as well as their extraordinary and ordinary refractive indices (n_e and n_o), are essential for the modulation of millimeter-wave, infrared, visible region. Among the application of them, phase shifters [**15-17**], attenuator, polarizers and wavelength selection filters [**18-20**] have been demonstrated.

Composed of 4-cyano-4'-n-pentyl-biphenyl (5CB), 4-cyano-4'-nheptyl-biphenyl (7CB), 4-cyano-4'-n-octyloxy-biphenyl (8OCB) and 4-cyano-4''-n-pentyl-p-terphenyl (5CT), the eutectic liquid crystal (LC) mixture E7, has been widely used in LC devices due to its large birefringence and wide nematic temperature range (-10°C~59°C). In order to pushing THz technology, the electro-optical phase shifters and filters in this region are all in high demand. Recently, E7-based voltage-controlled phase shifter, tunable Solc filter and tunable Lyot filter

in THz range have been reported [**17,21,22**].

1.4 Thesis highlight

In Chapter 2, the experimental methods and sample preparation of PC antennas are described. For experimental setup, the THz-Time-domain Spectroscopy (THz-TDS), the temperature and humidity controlled system are introduced in detail. The temperature of the E7 sample was controlled with a fluctuation less than 0.1°C. Besides, the basic theories about THz radiation generated from dipole antenna on pulse mode are mentioned.

In Chapter 3, we report the development of measuring LC's refractive indices in the recent years and the way of extraction of optical constants from THz-TDS we have used.

In Chapter 4, the results are analyzed and discussed, and we also compared the data with the visible range's in this section. In the last chapter, the conclusions will be mentioned.

Chapter 2 Experimental Methods

2.1 The Preparation of LC cell and reference cell

A homogeneously aligned LC cell and a reference cell, schematically shown in **Fig. 2.1**, were prepared in this work. The LC cell was constructed by sandwiching the LC (E7, Merck) between two fused silica optical-grade windows. Thickness of the liquid crystal layer was controlled with Mylar spacers and measured by subtracting the substrates thicknesses from the total cell thickness. The LC layer thickness in this work is d = 0.552 ± 0.002 *mm*. We achieved homogeneous alignment of the nematic LC by rubbing t he spin-coated polyimide films on the substrates. The temperature of the liquid crystal cell can be varied and controlled to ± 0.05°C. The reference cell was constructed by two fused silica windows with nominal thickness of 3.0 *mm* each and in contact to each other.

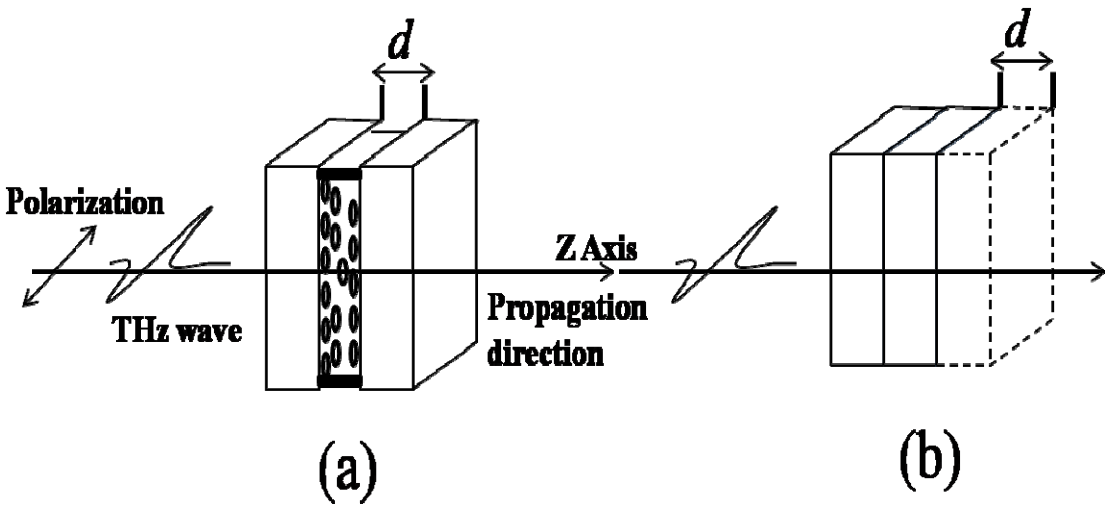

Fig. 2.1 Sketches of (a) LC cell and (b) the reference cell. The substrates are fused silica and the alignment of LC cell is homogeneous.

We showed the procedure of preparing the LC cell as **Fig. 2.2**:

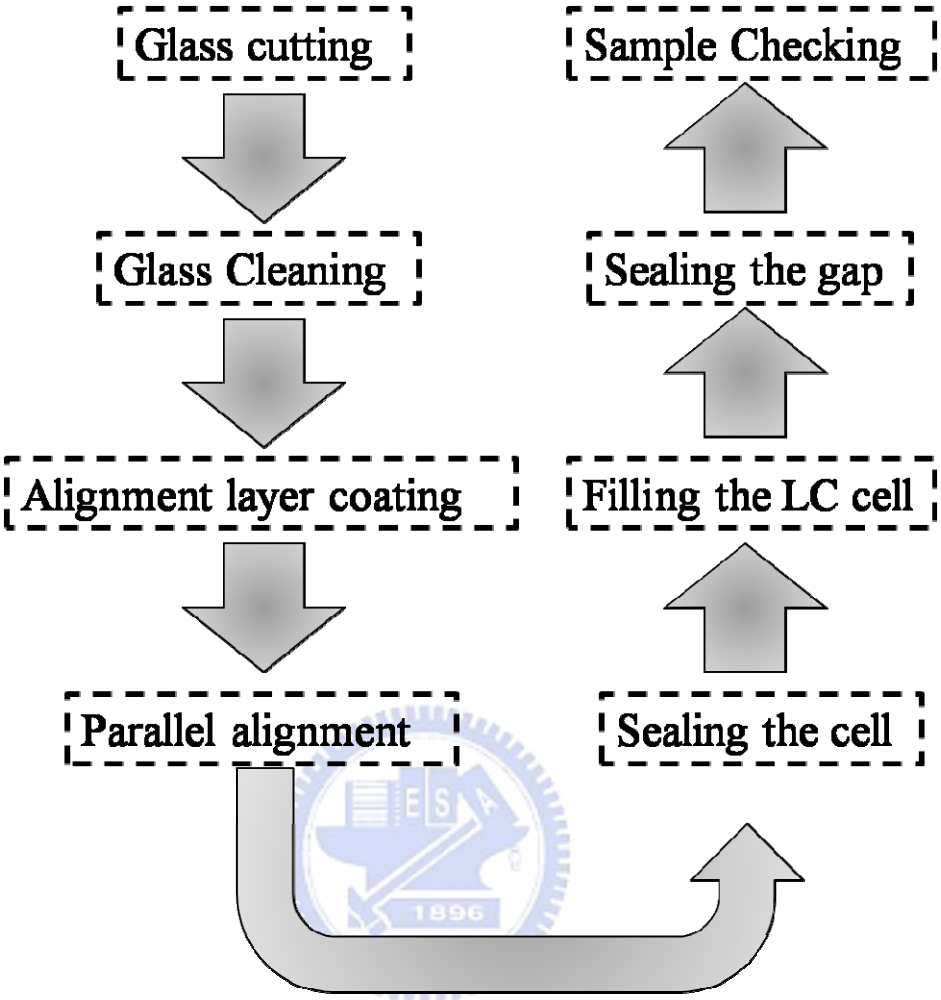

Fig. 2.2 the procedure of preparing the LC cell

Glass cutting:

1. Put on the gloves in order to avoid being pollute glasses and cut.
2. Choose fused silica glass or quartz glass.
3. Using the diamond knife-edge to cut the glasses.
4. Measure the thickness of the glasses by screw micrometer.

Glass cleaning:

1. Mount the glasses on Teflon foundation of the beaker; add water to surpass the glasses up to, and pour into the cleaner.

2. In order to eliminate the dusts and grimes on the glass, put the beaker into the supersonic oscillator and shake it for five minutes. After that, take it out and flush it by the distilled, then use the nitrogen to air-dry.

3. In order to eliminate the organism and oil-slick on the glasses, put the glasses into the beaker with acetone and shake it for five minutes.

4. In order to eliminate particles on the glasses, put the glasses into the beaker with methyl alcohol and shake it for five minutes.

5. Put the glasses into the beaker with pure water and shake it foe five minutes. The function of this step is for eliminating the residual solvent on the glasses.

6. After using nitrogen to air-dry, put the glasses into 120 degrees centigrade ovens in order to dry out the moisture.

Alignment layer coating and **Parallel alignment:**

1. Put the polyimide in the room temperature to warm for one hour.

2. Put the glasses on the spin coater, and use the burette to trickle the polyimide on the substrate. There are two steps when spining the glasses:

   (a) The first step: 2000 rpm (50 sec) (b) The second step: 4000 rpm (50 sec)

3. Put the glasses into 170 degrees centigrade ovens to dry for one hour.

4. Put the substrate coated the polyimide film on the rubbing machine, and make the effect of parallel alignment.

Sealing the cell:

1. In order to remove the pellet and dust on the substrate, use the nitrogen to blow the glasses

2. Assemble two glasses substrate plates and fix the cell with the clips.

3. Spread the AB glue all around in the sample, but leave a gap for filling the LC.

Filling the LC cell and **Sealing the gap:**

1. The cell gap is enough wide, vacuum is not necessary. Drip LC into the cell directly, and pay attention that do not produce bubbles.

2. Seal the gap by using AB glue.

Sample checking:

1. Observe the sample outward appearance, whether the LC leak off.

2. Measure the sample thickness by screw micrometer

3. There is a simple way for sample checking, we put the NLC sample among cross polarizer, if aligned effect is good, we can discover slightly light to shade change when rotating the cell. I will show it as follows:

A set of crossed polarizer is placed before and after the LC sample, respectively. If aligned effect is good, we can discover slightly light to shade change when rotating the cell.

First, we define the original coordinate for the polarization of polarizer and another new coordinate for the optical axis of the LC sample, respectively. Between the two coordinates, there is an angle θ shown as **Fig. 2.3**:

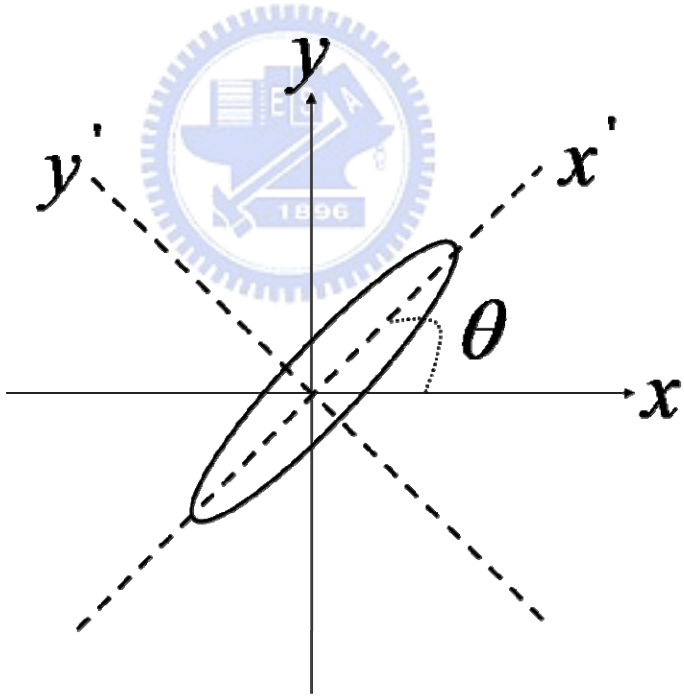

Fig. 2.3 The conversion of the original coordinate (x, y) and the new coordinate (x', y')

From the Jones Matrix, we can define the electric field passing through the polarizer is :

$$E_P = \begin{bmatrix} E_x \\ E_y \end{bmatrix} = E_0 \begin{bmatrix} 1 \\ 0 \end{bmatrix}_{xy} \tag{2.1}$$

We convert the original coordinate into the new coordinate, and showing as **Eq. (2.2)**:

$$\mathrm{E}'_{LC} = E_0 \begin{pmatrix} \cos\theta & \sin\theta \\ -\sin\theta & \cos\theta \end{pmatrix} \begin{pmatrix} 1 \\ 0 \end{pmatrix} = E_0 \begin{pmatrix} \cos\theta \\ -\sin\theta \end{pmatrix}_{X'Y'} \tag{2.2}$$

After changing the coordinate of reference, the electric field passing through the LC sample can be described as **Eq. (2.3)**:

$$\mathrm{E}'_{LC} = E_0 \begin{pmatrix} e^{in_e kd} & 0 \\ 0 & e^{in_o kd} \end{pmatrix} \begin{pmatrix} \cos\theta \\ -\sin\theta \end{pmatrix} = E_0 \begin{pmatrix} e^{in_e kd}\cos\theta \\ -e^{in_o kd}\sin\theta \end{pmatrix} \tag{2.3}$$

Here, we have to convert the Jones matrix into the original coordinate, and we will derive the **Eq. (2.4)**:

$$\mathrm{E}_{LC} = E_0 \begin{pmatrix} \cos\theta & -\sin\theta \\ \sin\theta & \cos\theta \end{pmatrix} \begin{pmatrix} e^{in_e kd}\cos\theta \\ -e^{in_o kd}\sin\theta \end{pmatrix} = E_0 \begin{pmatrix} e^{in_e kd}\cos^2\theta + e^{in_o kd}\sin^2\theta \\ e^{in_e kd}\cos\theta\sin\theta - e^{in_o kd}\sin\theta\cos\theta \end{pmatrix} \tag{2.4}$$

After passing through the analyzer, the electric field will just exist the y direction, and the result is shown as **Eq. (2.5)**:

$$\mathrm{E}_A = E_0 \begin{pmatrix} 0 & 0 \\ 0 & 1 \end{pmatrix} \begin{pmatrix} e^{in_e kd}\cos^2\theta + e^{in_o kd}\sin^2\theta \\ e^{in_e kd}\sin\theta\cos\theta - e^{in_o kd}\sin\theta\cos\theta \end{pmatrix} = E_0 \begin{pmatrix} 0 \\ e^{in_e kd}\sin\theta\cos\theta - e^{in_o kd}\sin\theta\cos\theta \end{pmatrix}_{XY} \tag{2.5}$$

If we define the $\bar{n} = \frac{n_{//} + n_{\perp}}{2}$ and $\Delta n = n_{//} - n_{\perp}$, the electric field of y will be derive as **Eq. (2.6)**:

$$\begin{aligned} \vec{\mathrm{E}}_A &= E_0 e^{in_e kd}\sin\theta\cos\theta - e^{in_o kd}\sin\theta\cos\theta\ \hat{\mathrm{y}} = E_0 e^{i\bar{n}kd}\sin\theta\cos\theta(e^{i\frac{\Delta n}{2}kd} - e^{-i\frac{\Delta n}{2}kd})\ \hat{\mathrm{y}} \\ &= E_0 e^{i\bar{n}kd}\sin\theta\cos\theta(2i\sin\frac{\Delta nkd}{2})\ \hat{\mathrm{y}} \end{aligned} \tag{2.6}$$

From the information of electric field, we can derive the optical intensity as **Eq. (2.7)**:

$$I = \left|\vec{\mathrm{E}}_A\right|^2 = I_0 \sin^2(2\theta)\sin^2(\frac{\Delta\Phi}{2}) \tag{2.7}$$

Here, I_0 is the intensity of incident light, θ is the angle between the polarizer and the optical axis of the LC sample, and $\Delta\Phi$ is the phase shift caused by passing through the LC

sample. From **Eq. (2.7)**, we know that the optical intensity is the highest as θ is 45°, and we also can find the lowest intensity as θ is 0°.

2.2 Temperature and humidity controlled system

In order to obtain the temperature dependence of the LCs' refractive indices, an accuracy temperature controlled system is necessary. We put the cell in a copper box, which has two open windows for THz wave passing. The copper box was covered by Teflon with the thickness of 0.5cm for keeping the temperature inside. The copper box also has two small holes with the diameter of 3.0 mm for resistant type temperature probes (YSI 423, Yellow Springs Instrument Co., Inc.) and two larger holes with 1.0-cm-diameter for cylinder current heaters. One of the probe and two heaters were connected to a temperature controller (YSI Model 72, Yellow Springs Instrument Co., Inc.) in order to set the temperature of the cells. Another probe, which directly contacts the cell was connected to a voltage multimeter for probing the actual cell temperature by reading the resistance of the probe. **Fig 2.4** shows the pictures of the temperature controlled sample holder. **Fig. 2.5** is shown the temperature controller and the probe, respectively. The fluctuation of the temperature of the cell is less than 0.04°C. The testing data is shown in **Fig. 2.6**. This temperature control system was employed in this work for providing a stable temperature control of the LC cells and the reference cells.

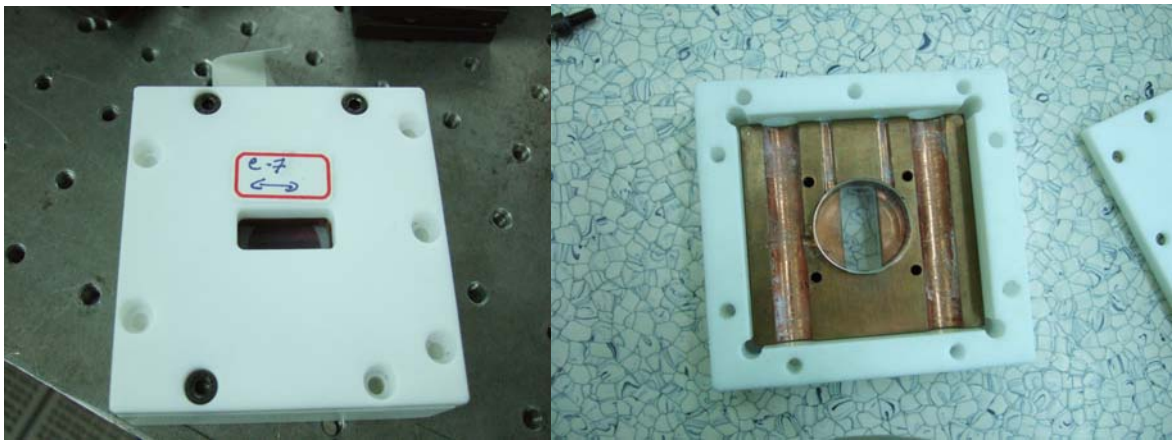

Fig. 2.4 The pictures of the temperature-controlled sample holder, which consists with a copper oven (inside) and a Teflon cover (outside).

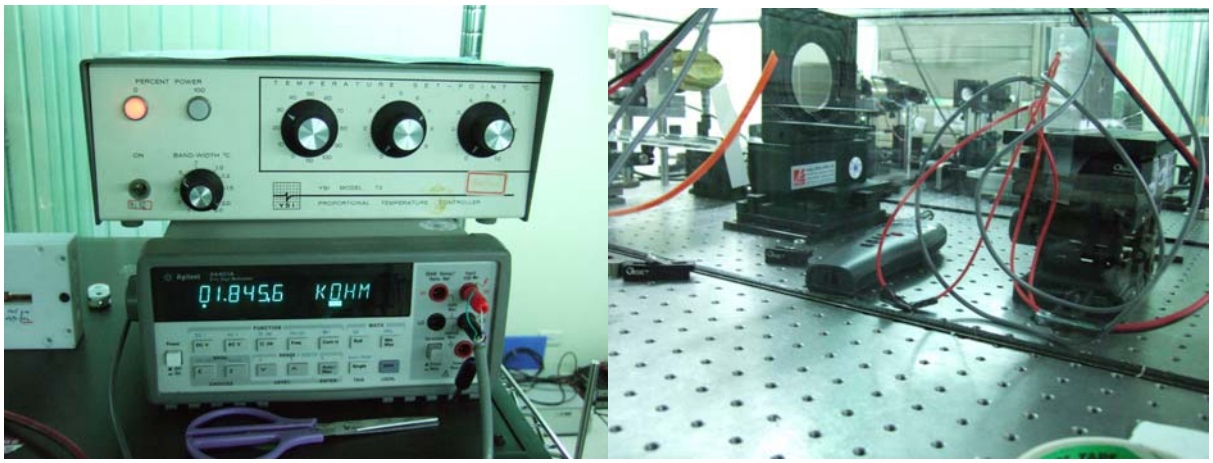

Fig. 2.5 The pictures of the temperature controller and the probe (YSI 423, Yellow Springs Instrument Co., Inc.)

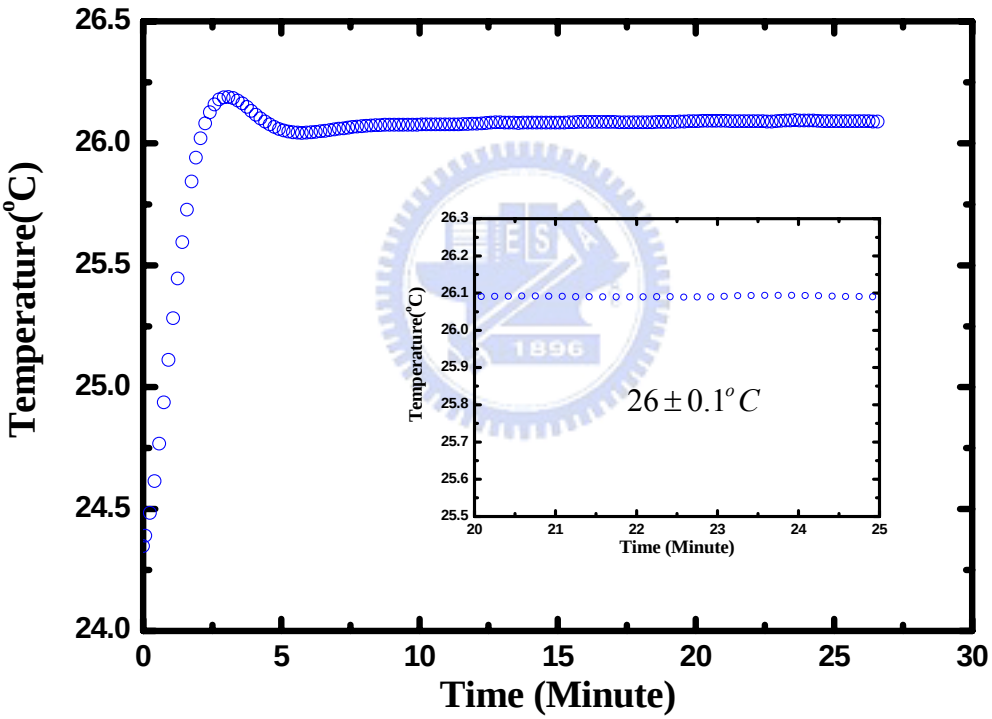

Fig. 2.6 The testing result which is set at $26^{o}C$ of the temperature control system.

There are several absorption lines of water in the range of 0.2 to 1.5 THz [**23**]. We found that those water lines will affect the accuracy of the measured results. According to this, a dry environment is necessary for obtaining accurate results. We used acrylic plates to make a box, which covers whole THz system to approach a close system. The THz-TDS was purged with dry nitrogen so that it could maintain at a relative humidity of (4.0 ± 0.5) %. **Fig. 2.7(a)** and **2.7(b)** show the THz temporal profile and the frequency spectra after purging, respectively. From the **Fig. 2.7(b)**, the determination of Signal-Noise-Ratio can reach 10^6 for certain.

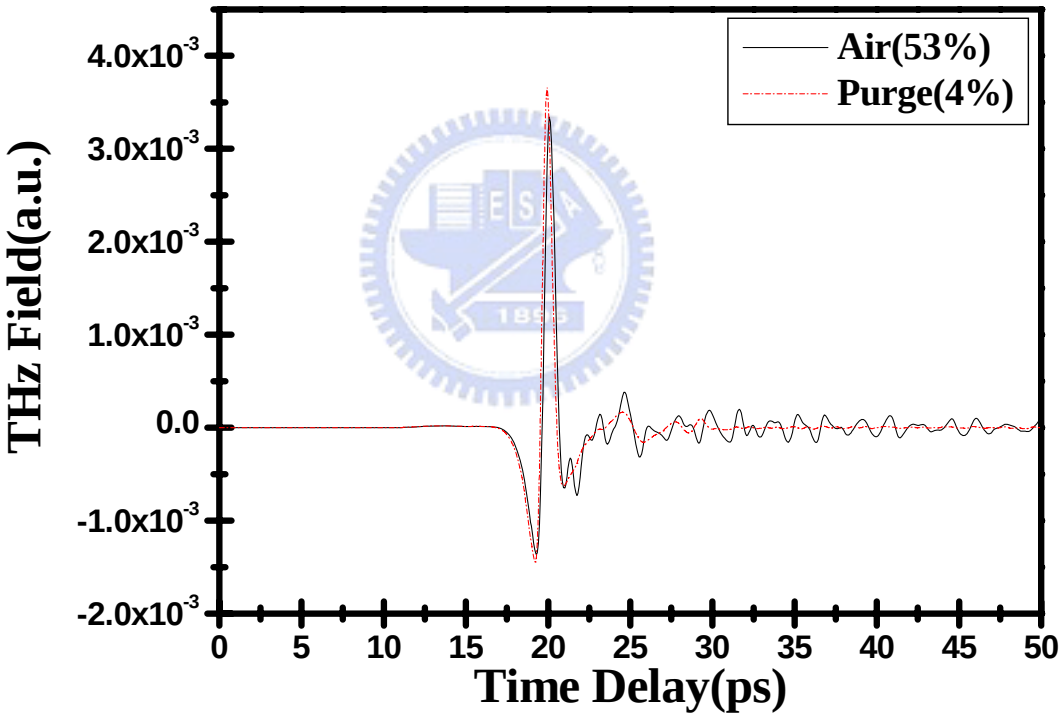

Fig. 2.7(a). Temporal profiles of THz before (solid line) and after (dash line)purging.The relative humidities before and after purging are 53% and 4%, respectively.

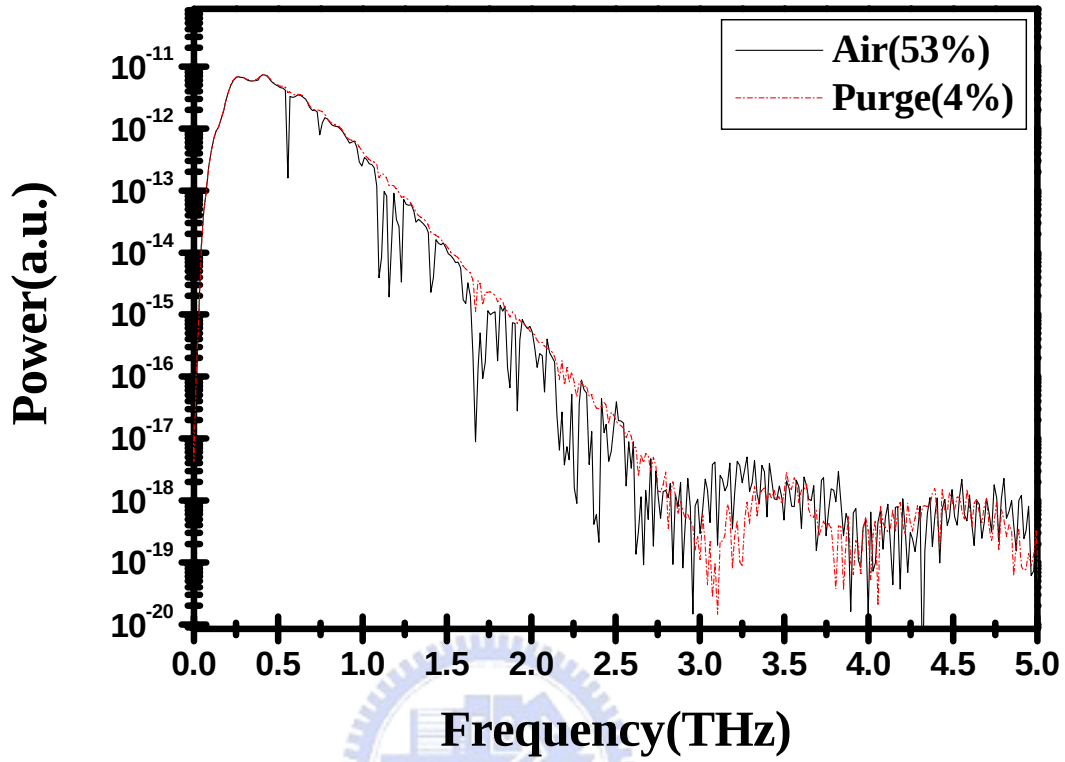

Fig. 2.7(b). Frequency domain of THz before (solid line) and after (dash line)purging.The relative humidities before and after purging are 53% and 4%.

2.3 THz Time-domain spectroscopy (THz-TDS)

2.3-1 Introduction

Characterization of LCs and LC devices in the THz frequency range are performed using THz time-domain spectroscopy (TDS) [**5**]. THz-TDS is a powerful technique that allows broadband THz generation and detection of the field amplitude and phase of the THz wave. A schematic representation of our setup is depicted in **Figure 2.8**. The light source is a mode-lucked femtosecond Ti:sapphire laser (Spectra Physics Tsunami). The pulses are split into two beams; one constitutes the so-called pump or excitation beam, the other is referred as the probe beam. The pump pulses impinged on a low-temperature grown Gallium Arsenide

(LT-GaAs) photoconductive dipole antenna, acts as a THz emitter. The generated THz pulses are collected and guided by gold-coated parabolic mirrors onto the sample. The incident THz waves on the sample can be also focused by another parabolic gold mirror. The transmitted pulses from the sample are focused by another parabolic gold mirror onto the THz detector, which in our case is also a photoconductive antenna.

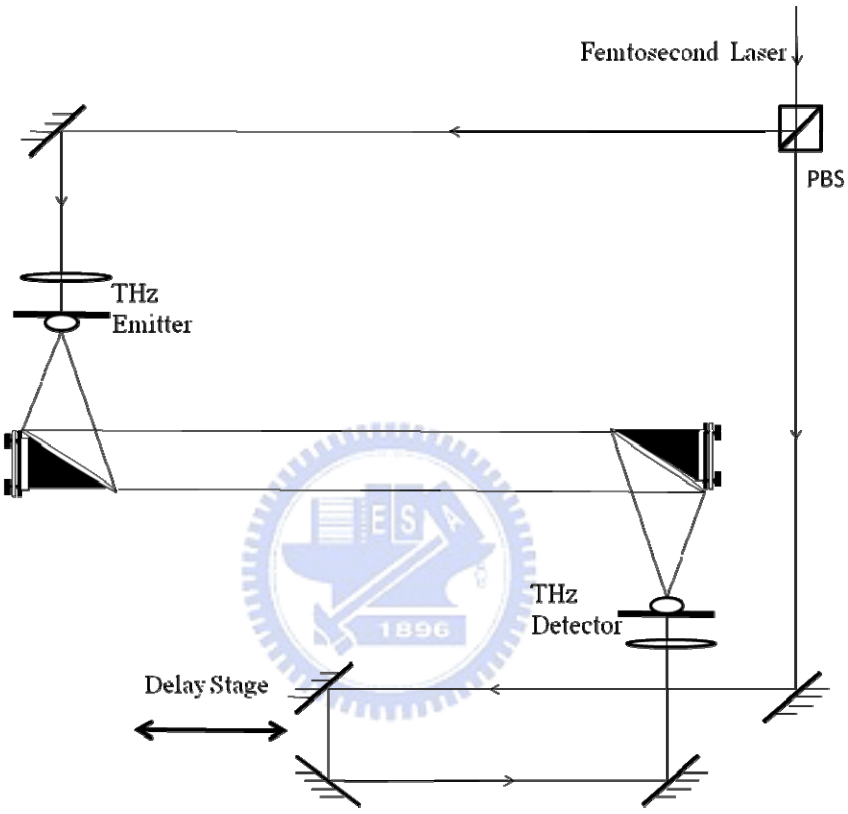

Figure 2.8 The general setup of the antenna-based time domain spectroscopy system

2.3-2 Theory of generating THz radiation

Many groups have made great efforts to develop THz radiation sources in both continuous – wave and pulsed way. Free-Space Electron Laser [**24,25**], and backward wave oscillators [**26**] are electron beam sources that generate relatively high power signals at the THz region. By injecting a CO_2 pump laser light into a cavity filled with a gas that lases, one

also can obtain THz radiation [**27,28**], and the lasing frequency is fixed dictated by the filling gas. In our experimental methods, the optical rectification and resonant THz radiation in photoconductor generated by a pulse laser are used. Here, the two methods will be introduced as follows, respectively.

2.3-2-1 Optical rectification

One of methods to generation THz. is to make use of the Free-Space Electro-Optic Sampling (FSEOS) which based on an emission of optical rectification [**29,30**]. This effect as shown in **Fig. 2.9** arises from the second ordered susceptibility χ of nonlinear crystals. The susceptibility, $\chi = P / \varepsilon_0 E$ measures the degree of polarization which caused by an electric field applied to a dielectric material. Optical rectification in a non-absorbing medium is a process in which a laser pulse creates a time-dependent polarization that radiates an electric field which can be written as $\vec{E}(t) \propto \frac{\partial^2 \vec{P}}{\partial t^2}$ in the far field, where the polarization P follows the pulse intensity envelope. It is called rectification because the rapid oscillations of the electric field of the pulse laser are "rectified" and only the envelope of the oscillations remains. In a material subjected simultaneously to waves of frequencies w_1 and w_2, the P will include the form of $\cos(w_1 t)\cos(w_2 t) = \left[\cos(w_1 + w_2)t + \cos(w_1 - w_2)t\right]/2$. Thus both sum and difference frequencies as a result of the beats that form between the different frequencies will be generated [**31**]. The THz pulses consist of a broad range of spectrum, from zero up to the bandwidth of the visible region, and bandwidth as large as 30THz has been obtained using this generation mechanism. On the other hand, FSEOS has typically lower power because the

power of THz pulse comes from the incident laser pulses entirely.

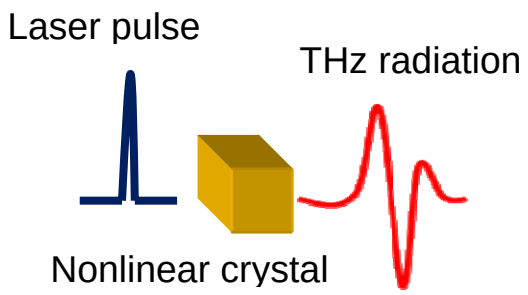

Figure 2.9 Optical rectification

2.3-2-2 Photoconductive(PC) switch

Biased PC switch can be used to generate THz radiation. It is generally based on the "current surge model" [**32**] which will be discussed in detail in the next chapter. According to this model, as the energy of the input laser is higher than the energy of bandgap of photoconductor, then electron-hole pairs are excited and the mechanism to generated THz radiation can occur. Semiconductor such as GaAs (Eg=1.43eV), with the surface bands of a semiconductor lie within the energy produced by input photon and thus Fermi-level pinning occurs, leading to band bending and formation of a depletion region.

In briefly, the electromagnetic field of THz radiation is generated from a transient current which is generated on the surface of the photoconductor. Carriers are generated by the pulse laser instantaneously. In order to accelerate the carriers we add bias across the PC antenna. Then, the resultant transient current, or called current surge, produces an electric field on the surface of the photoconductor. This surface electric field is regarded as the source of the THz radiation. **Figure 2.10** shows the setup for this method.

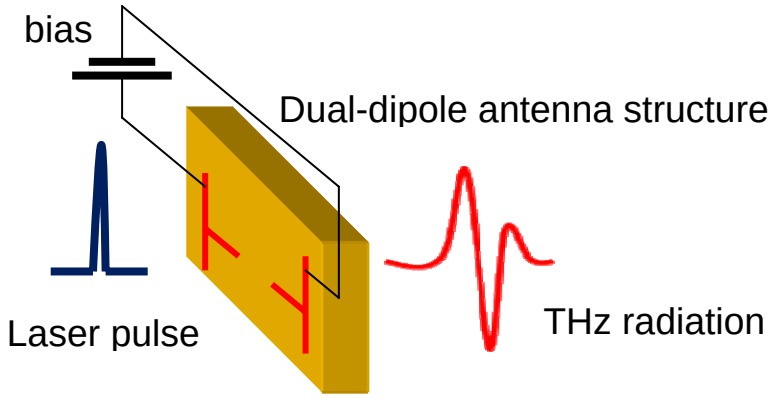

Figure 2.10 Photoconductive switch

2.3-2-3 Current-surge model

The first step, there are some time-average parameters which we need to define the THz radiation [**33**].

Charge density $\Rightarrow \rho(x,y,z,t)$

Current density $\Rightarrow \vec{J}(x,y,z,t)$

Electric field intensity $\Rightarrow \vec{E}(x,y,z,t)$

Magnetic flux density $\Rightarrow \vec{B}(x,y,z,t)$

Then, it is necessary to construct Maxwell's equation for current-surge model. According to Maxwell's equation [**34**]:

$$\nabla \times \vec{E} = -\frac{\partial \vec{B}}{\partial t} \quad \text{(Faraday's Law)} \tag{2.8}$$

$$\nabla \cdot \vec{E} = \frac{\rho}{\varepsilon} \quad \text{(Gauss Law)} \tag{2.9}$$

$$\nabla \times \vec{H} = \vec{J} + \frac{\partial \vec{D}}{\partial t} \quad \text{(Ampere's Law)} \tag{2.10}$$

$$\nabla\cdot\vec{B}=0 \tag{2.11}$$

And we know

$$\vec{B}=\nabla\times\vec{A} \tag{2.12}$$

From **Eq. (2.8)** and **(2.12)**, we can obtain:

$$\nabla\times\vec{E}=-\frac{\partial\vec{B}}{\partial t}=-\frac{\partial}{\partial t}\left(\nabla\times\vec{A}\right)=\nabla\times\left(-\frac{\partial\vec{A}}{\partial t}\right) \quad \Rightarrow \nabla\times\left(\vec{E}+\frac{\partial\vec{A}}{\partial t}\right)=0 \tag{2.13}$$

Then, we set a non-vector value V and employ that $\nabla\times\nabla V=0$ to substitute the **Eq. (2.13)**.

$$-\nabla V=\vec{E}+\frac{\partial\vec{A}}{\partial t} \Rightarrow \vec{E}=-\nabla V-\frac{\partial\vec{A}}{\partial t} \tag{2.14}$$

From **Eq. (2.10)**、**(2.12)** and $\vec{H}=\frac{\vec{B}}{\mu}$、$\vec{D}=\varepsilon\vec{E}$,we obtain

$$\frac{\nabla\times\vec{B}}{\mu}=\vec{J}+\varepsilon\frac{\partial\vec{E}}{\partial t} \Rightarrow \nabla\times\left(\nabla\times\vec{A}\right)=\mu\left(\vec{J}+\varepsilon\frac{\partial\vec{E}}{\partial t}\right) \tag{2.15}$$

Substitute **Eq. (2.14)** into **Eq. (2.15)**

$$\nabla\times\left(\nabla\times\vec{A}\right)=\mu\left[\vec{J}+\varepsilon\frac{\partial}{\partial t}\left(-\nabla V-\frac{\partial\vec{A}}{\partial t}\right)\right]$$

$$\nabla\left(\nabla\cdot\vec{A}\right)-\nabla^2\vec{A}=\mu\vec{J}-\mu\varepsilon\nabla\frac{\partial V}{\partial t}-\mu\varepsilon\frac{\partial^2\vec{A}}{\partial t^2}$$

$$\Rightarrow \nabla^2\vec{A}-\mu\varepsilon\frac{\partial^2\vec{A}}{\partial t^2}=-\mu\vec{J}+\nabla\left(\nabla\cdot\vec{A}+\mu\varepsilon\frac{\partial V}{\partial t}\right) \tag{2.16}$$

From **Eq. (2.9)** and $\vec{D}=\varepsilon\vec{E}$

$$\nabla\cdot\left(\varepsilon\vec{E}\right)=-\nabla\cdot\left[\varepsilon\left(\nabla V+\frac{\partial\vec{A}}{\partial t}\right)\right]=\rho$$

$$\Rightarrow \nabla^2 V + \frac{\partial}{\partial t}\left(\nabla \cdot \vec{A}\right) = -\frac{\rho}{\varepsilon} \tag{2.17}$$

Due to Lorentz gauge assumption $\nabla \cdot \vec{A} + \varepsilon\mu \frac{\partial}{\partial t} V = 0$, **Eq. (2.16)** becomes as

$$\nabla^2 \vec{A} - \mu\varepsilon \frac{\partial^2 \vec{A}}{\partial t^2} = -\mu \vec{J} \tag{2.18}$$

And, **Eq. (2.17)** can be written as

$$\nabla^2 V - \mu\varepsilon \frac{\partial^2 V}{\partial t^2} = -\frac{\rho}{\varepsilon} \tag{2.19}$$

Eq. (2.18) and **(2.19)** are the two inhomogeneous wave equations written in terms of $\vec{A}$ and V. The two wave equations are used to determine a functional and time dependent of the radiated electric field in the far field.

From **Eq. (2.10)**, the continuity equation of the free carriers is obtained.

$$\nabla \cdot \left(\nabla \times \vec{H}\right) = \nabla \cdot \left(\vec{J} + \frac{\partial \vec{D}}{\partial t}\right) = \nabla \cdot \vec{J} + \frac{\partial \rho}{\partial t} = 0 \tag{2.20}$$

In the fact, the current density of the photoconductor antenna which adds the bias is the transverse current, parallel the surface of the PC antenna and perpendicular the direction of propagation. So that

$$\nabla \cdot \vec{J} = 0 \tag{2.21}$$

From **Eq. (2.20)** and **(2.21)**, we can deduce that the charge density does not vary with time and not contribute the time dependent radiated electric field. As the result, **Eq. (2.14)** becomes

$$\vec{E}\left(\vec{r},t\right)=-\frac{\partial}{\partial t}\vec{A}(t) \tag{2.22}$$

The solution of the vector potential $\vec{A}$ in **Eq. (2.18)** leads into the **Eq. (2.22)** to express the time dependent radiated electric field $\vec{E}_{rad}(\vec{r},t)$ at the displacement $\vec{r}$ from the center of the PC antenna.

$$\vec{E}_{rad}(\vec{r},t)=-\frac{1}{4\pi\varepsilon_0 c^2}\frac{\partial}{\partial t}\int\frac{\vec{J}_s\left(\vec{r}',t-\frac{\left|\vec{r}-\vec{r}'\right|}{c}\right)}{\left|\vec{r}-\vec{r}'\right|}da' \tag{2.23}$$

where ε_0 is the permittivity of free space, c is the speed of light in vacuum, $\vec{J}_s$ is the surface current of the PC antenna in the retarded time, and da' is the increment of surface area at the displacement $\vec{r}'$ from the center of the PC antenna. The integration is covered with whole the optically illuminated area of the PC antenna. In the far field,

$$\left|\vec{r}-\vec{r}'\right|=r\left(1-\frac{\hat{n}\cdot\vec{r}'}{r}\right)\approx r \tag{2.24}$$

The gap between the electrodes of the PC antenna is assumed to be uniformly illuminated by the optical source. Therefore, the surface current $\vec{J}_s$ can be set as a constant in space. Then, the radiated electric field in **Eq. (2.23)** can be written as

$$\vec{E}_{rad}(\vec{r},t)=-\frac{1}{4\pi\varepsilon_0 c^2}\frac{A}{r}\frac{\partial}{\partial t}\vec{J}_s\left(t-\frac{r}{c}\right) \tag{2.25}$$

where A is the illuminated area of the PC antenna and $r=\sqrt{x^2+y^2+z^2}$ .We considered that the THz radiation is generated on Z axis (i.e. x = y = 0), and let $t\rightarrow t-\left(\frac{z}{c}\right)$. Thus, The **Eq. (2.25)** can be written as

$$\vec{E}_{rad}(\vec{r},t)=-\frac{1}{4\pi\varepsilon_0 c^2}\frac{A}{z}\frac{\partial}{\partial t}\vec{J}_s\left(t\right) \tag{2.26}$$

Beside, we can know the **Eq. (2.27)** from surface current [**35**].

$$\vec{J}_s(t) = \frac{\sigma_s(t)\vec{E}_b}{\frac{\sigma_s(t)\eta_0}{1+n}+1} \tag{2.27}$$

where n is the refractive index of photoconductor antenna under the wavelength of μm. η_0 is the impedance in free space, and $\sigma_s(t)$ is the surface conductivity which is shown in the **Eq. (2.28)**.

$$\sigma_s(t) \equiv \frac{e(1-R)}{\hbar w}\int_{-\infty}^{t} dt' m(t,t') I_{opt}(t') \exp[\frac{-(t-t')}{\tau_{car}}] \tag{2.28}$$

where e is the electric charge, R is the reflectivity of photoconductor antenna, $\hbar w$ is the photon energy, $m(t,t')$ is the time-dependent carrier mobility at time t from created carrier at time t', I_{opt} is the time-dependent of optical intensity, and τ_{car} is the carrier lifetime of excited carriers. For the present derivation, we assume that carrier mobility is a constant.

$$m(t,t') = m \tag{2.29}$$

And assume that the carrier lifetime is long enough, $\tau_{car} \to \infty$. A Gaussian intensity profile of the optical beam is assumed:

$$I_{opt}(t') = I_0 \exp(\frac{-t'^2}{\tau^2}) \tag{2.30}$$

From these assumptions, the surface conductivity becomes

$$\sigma_s(t) \equiv \frac{e(1-R)}{\hbar w} I_0 \int_{-\infty}^{t} dt' m \exp(\frac{-t'^2}{\tau^2}) \tag{2.31}$$

From the **Eq. (2.29)** lead to the **Eq. (2.26)**.

$$\vec{E}_{rad}(\vec{r},t) = -\frac{1}{4\pi\varepsilon_0 c^2}\frac{A}{z}\frac{e(1-R)}{\hbar w} I_0 m \exp(\frac{-t^2}{\tau^2}) \times \left[1 + \frac{\eta_0 e(1-R) I_0 m}{(n+1)\hbar w}\int_{-\infty}^{t/\tau} \tau \exp(-x^2) dx\right]^{-2} \tag{2.32}$$

Comparing with the result from experiment, it is necessary to rewrite the Eq. (2.30) in term of the experimental parameters E_b which is the bias electric field applied across the

photoconductor, and F_{opt} which is the incident optical intensity.

$$F_{opt} = \int_{-\infty}^{\infty} I_0 \exp(\frac{-t^2}{\tau^2})dt = \sqrt{\pi} I_0 \tau \equiv \frac{E_{opt}}{A} \tag{2.33}$$

Where E_{opt} is the average optical energy and A is the area of the incident optical beam. Then we define the parameter B and D to simplify the equation.

$$B = \frac{Ae(1-R)m}{4\pi\varepsilon_0 c^2 z\hbar w\sqrt{\pi}} \tag{2.34}$$

$$D = \frac{\eta_0 e(1-R)m}{(n+1)\hbar w\sqrt{\pi}} \tag{2.35}$$

And then, the electric field in the far field can be written as

$$E_{rad}(t) = -BE_b \frac{F_{opt}}{\tau} \exp(\frac{-t^2}{\tau^2}) \times \left[1 + DF_{opt} \int_{-\infty}^{t/\tau} \exp(-x^2)dx\right]^{-2} \tag{2.36}$$

Beside of current surge model, we can also discuss on the point of the carrier dynamics in semiconductor to analyze the THz generation by Drude-Lorentz model when we need to discuss the factor of material in PC antenna [**36,37**].

2.3-2-4 Drude-Lorentz model

For the calculation of carrier transport and THz radiation in a biased semiconductor, the one-dimensional Drude-Lorentz model is used. When a biased semiconductor is pumped by a laser pulse with photon energies greater than the band gap of the semiconductor, electrons and holes will be created in the conduction band and valence band, respectively. The carrier pumped by ultrashort laser pulse is trapped in the mid-gap states with the time constant of the carrier trapping time. The time-dependence of carrier

density is given by the following equation.

$$\frac{dn(\mathrm{t})}{dt} = -\frac{n(\mathrm{t})}{\tau_{\mathrm{c}}} + G(\mathrm{t}) \tag{2.37}$$

Where n(t) is the density of the carrier, G(t) is the generation rate of the carrier by the laser pulse, and τ_{c} is the carrier trapping time. The generated carriers will be accelerated by the bias electric field. The acceleration of electrons (holes) in the electric field is given by

$$\frac{d\nu_{e,h}(\mathrm{t})}{dt} = -\frac{\nu_{e,h}(\mathrm{t})}{\tau_s} + \frac{q_{e,h}}{m_{e,h}} E \tag{2.38}$$

Where $\nu_{e,h}(\mathrm{t})$ is the average velocity of the carrier, $q_{e,h}$ is the charge of an electron (a hole), $m_{e,h}$ is the effective mass of the electron (hole), $\tau_{e,h}$ is the momentum relaxation time, and E is the local electric field. The subscript e and h represent electron and hole, respectively. The local electric field E is smaller than the applied bias electric field E_b due to the screening effects of the space charges,

$$E = E_b - \frac{P}{\alpha\varepsilon} \tag{2.39}$$

Where P is the polarization induced by the spatial separation of the electron and hole, ε is the dielectric constant of the substrate and α is the geometrical factor of the PC material. The geometrical factor α is equal to three for an isotropic dielectric material. It is noted that both, the free and trapped carriers contribute to the screening of the electric field. The time dependence of polarization P can be written as

$$\frac{dP}{dt} = -\frac{P}{\tau_r} + J \tag{2.40}$$

Where τ_r is the recombination time between an electron and hole. In the Eq. (2.38), J is the density of the current contributed by an electron and hole,

$$J = en\nu_h - en\nu_e \tag{2.41}$$

Where e is the charge of a proton. The change of electric currents leads to electromagnetic radiation according to Maxwell's equations. In a simple Hertzian dipole theory, the far-field of the radiation E_{THz} is given by

$$E_{THz} \propto \frac{\partial J}{\partial t} \tag{2.42}$$

To simplify the following calculations, we introduce a relative speed ν between an electron and hole,

$$\nu = \nu_h - \nu_e \tag{2.43}$$

Then the electric field of THz radiation can be expressed as

$$E_{THz} \propto e\nu \frac{\partial n}{\partial t} + en\frac{\partial \nu}{\partial t} \tag{2.44}$$

The first term on the right hand side of the **Eq. (2.42)** represents the electromagnetic radiation due to the carrier density change, and the second term represents the electromagnetic radiation which is proportional the acceleration of the carrier under the electric field.

2.3-3 Theory of detecting THz radiation

One of detecting THz radiation ways is using PC antenna [**38**]. The detection principle of

PC antennas is the inversion of the THz generation because the photocarriers detected as a current are accelerated by the electric field of incident THz radiation instead of the bias voltage. The photocurrent response is the convolution of the optical pulse duration and the impulse current of the photoswitch across the photoconductive antenna on pulse mode. The photocurrent at a time delay *t* is shown as the following **Eq. (2.40)**:

$$J(t) = e\mu \int_{-\infty}^{\infty} E(\tau) N(\tau - t) d\tau \tag{2.40}$$

Where $N(\tau)$ is the number of photocreated carrier, and $E(\tau)$ is the incident electric field of the THz radiation.

There are two factors determine the spectral bandwidth in this detector. One of them is the photocurrent response (i.e. carrier lifetime) and the other one is the frequency dependence of the antenna structure [**39,40**]. In general, the low frequency cutoff of the detectors results from the collection efficiency of the dipole, while the upper frequency limit is determined by the photocarrier response.

2.3-4 Antenna-based emitter and detector

While the THz transmitter and receiver designs were identical in early THz TDS works, a wide range of different structures have been investigated, and optimized either for maximum signal or maximum bandwidth. Grischkowsky and coworkers pioneered the coplanar strip line for use as a THz emitter. This structure is appealing for both of the simplicity of the design and the extremely broad emission band [**41**].

The most commonly used THz receiver design has been a simple dipole antenna, roughly

50μm in length [**5**]. The collection sensitivity and radiation efficiency of the antenna both vary inversely with the wavelength. Thus, smaller dipole antennas provide a broader bandwidth response; dipoles as small as 30μm have been used. Of course, this 1/λ dependence no longer apply when the radiation wavelength in the substrate becomes comparable to the dipole length, so the details of the high frequency response are more complex. In addition, the low frequency roll-off in these quasi-optical systems is typically limited by diffraction effects due to the finite size of optical elements such as the substrate lenses. As a consequence, the 1/λ dependence may apply over only a rather limited spectral range. A detail analysis of THz-TDS system can accurately predict the measured spectral response, as long as all of these effects are taken into account.

If very small dipole antennas are used for both emission and detection, the high frequency limit is mainly determined by the temporal response of the system [**30,42,43**]. Another important limitation factor is the response time of the photoconductive material used for substrates of the THz antennas. This limit is more pronounced in the receiver antenna, since one does not expect the highest measured frequency to exceed the inverse of the temporal width of the photo-generated sampling gate, this duration is limited by the carrier trapping time, although a number of schemes have been proposed to avoid this limitation [**44,45**].

It should be noted that it is possible to detect broadband THz radiation even using a photoconductivity antenna with a slow carrier lifetime. In this case, one relies not on the width of the sampling gate, but merely on its fast-rising edge. If the photocurrent can be modeled as a step function, then the detector operates as a fast sampling gate in an integrating mode, and the measured signal is proportional to the integral of the incident THz field [**44**]. In this configuration, the bandwidth is limited by the speed of the rising edge of the current, which is determined by the duration of the optical pulse, and by the RC time constant of the

antenna [**46**].

2.3-5 THz-TDS with collimated beam system

For determination of the optical constants, we employ an antenna-based THz-TDS system with a collimated beam at the sample position [**47**]. A schematic of the experimental setup is shown in **Fig. 2.11**. Briefly, a mode-locked Ti: Sapphire laser (Spectra Physics, Tsunami, λ = 800 *nm*) generating 35 *fs* pulses at a repetition rate of 82 MHz with 400*mW* average output power is divided into two beams, one constitutes the so-called pump or excitation beam, the other is the probe beam. The former, with an average power of 35*mW* irradiated a low-temperature grown Gallium Arsenide (LT-GaAs) PC dipole antenna that was biased at 5V. The generated THz pulses, are collimated by a gold-coated parabolic mirrors onto the LC sample at normally incidence. The transmitted pulses from the sample are focused onto a detector which in our case is also a PC antenna by the second parabolic gold mirror. In order to make sure the polarization state of THz wave, a pair of parallel wire-grid polarizers was used before and after the LC cell respectively.

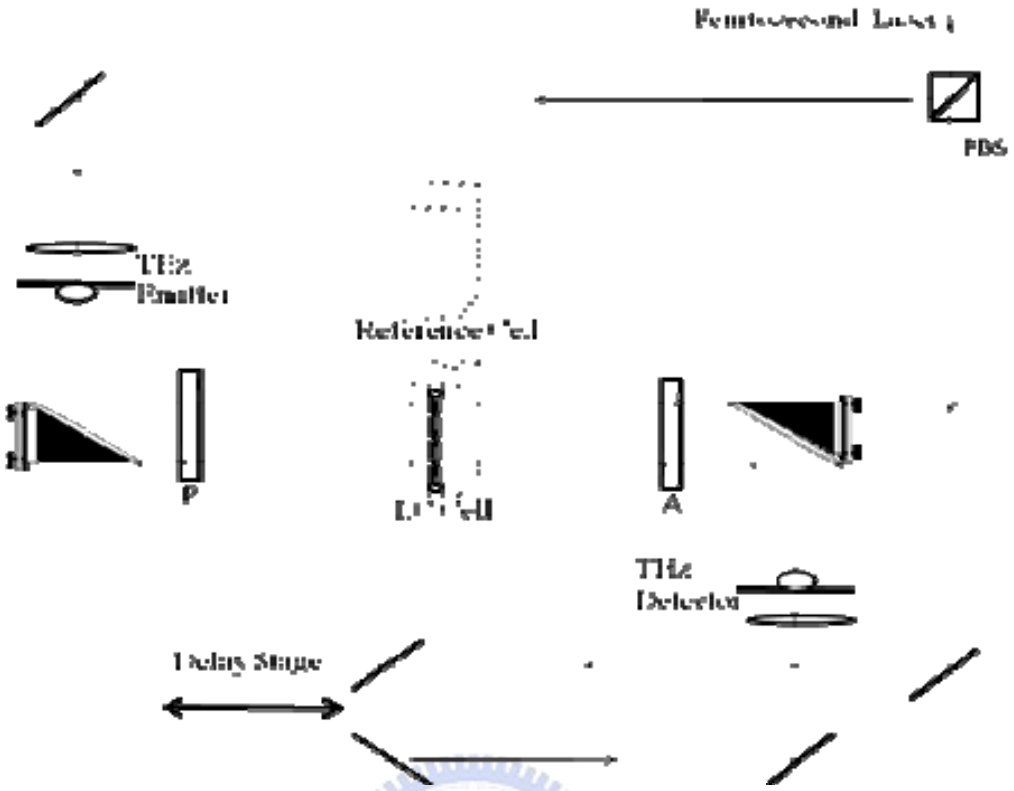

Fig. 2.11 Schematic of the THz-TDS. PBS: polarization beam splitter. P and A: THz polarizer and analyzer, respectively.

Chapter 3 Extraction of Optical Constants from THz Time-domain Spectroscopic Measurements

3.1 Introduction

Composed of 4-cyano-4'-n-pentyl-biphenyl (5CB), 4-cyano-4'-nheptyl-biphenyl (7CB), 4-cyano-4'-n-octyloxy-biphenyl (8OCB) and 4-cyano-4''-n-pentyl-p-terphenyl (5CT), the eutectic liquid crystal (LC) mixture E7, has been widely used in LC devices due to its large birefringence and wide nematic temperature range (-10°C~59°C).

In the visible frequency range, group of Wu et al. has proposed the refractive indices in the range of 450~656 *nm* [**48**], and the n_e increases from 1.73 to 1.80, while n_o varies from 1.52 to 1.54. In the near infrared (IR) region, the same author has offered Δn = 0.186 in the 1.55 μm [**49**]. After that, Brugioni et al. also studied Δn = 0.183 (n_e = 1.684, n_o = 1.500) in the same wavelength [**50**]. In the intermediate IR region, Wu et al. has also reported Δn increases from 0.18 to 0.19 in the frequengy range of 52~75 THz [**51**]. In the far IR region, both of Wu and Brugioni have introduced n_e = 1.69 and n_o =1.49 (Δn = 0.20) in the 10.6 μm [**49,52**]. In the microwave region, K. C. Lim et al. has found the Δn of E7 at the 30 GHz was 0.192, and the n_e and n_o were 1.790 and 1,598, respectively [**15**]. In the recent years, Yang and J. R. Sambles et al. have also investigated n_e =1.800 and n_o = 1.647 in the frequency range 26.5~40.0 GHz [53]. After that, n_e =1.78 and n_o = 1.65 were also determined in the 40~75 GHz by the same author [**54,55**]. Recently, by photomixing based on log periodic circularly toothed planar antenna, M. Koeberle et al. has reported n_e = 1.77, n_o = 1.64 (Δn = 0.13) at the 300 GHz [**56**].

These references mentioned we list in the **Table. 3.1**.

Above of all, the physical and chemical properties of E7 have been studied extensively, however, little research has been done between far IR and microwave (0.2 THz~1.4 THz).

Table. 3.1 The references measuring optical constants of E7 in different frequency range

Band	Wave length	Freq.	ne	no	Bire.	Ref.
Microwave	7.5~11.3 (mm)	26.5~40 (GHz)	1.800	1.647	0.153	Yang FZ, Applied Physics Letter 79 (22), 3717-3719, 2001
	10 (mm)	30(GHz)	1.79	1.598	0.192	K. C. Lim, Applied Physics Letter 62 (10), 1993
	5~7.5 (mm)	40~60 (GHz)	1.78	1.65	0.13	Yang FZ, Liquid Crystals 30 (5), 599-602, 2003
	4~6 (mm)	50~75 (GHz)	1.782	1.654	0.128	Yang FZ, Applied Physics Letter 81 (11), 2047-2049, 2002
	1 (mm)	300 (GHz)	1.77	1.64	0.13	M. Koeberle, T. Gobel
Far IR	10.21~ 10.768 (um)	27.9~ 29.4 (THz)	~	~	0.227	Shin-Tson Wu, Physical Review A, Vol 33, Number 2 (1986)
	10.6(um)	28.3 (THz)	1.691	1.493	0.198	Shin-Tson Wu, Journal of Applied Physics 97, 073501 (2005)
	10.6(um)	28.3 (THz)	1.694	1.495	0.199	S. Brugioni, Infrared physics & Technology 46, 17-21 (2004)

Far IR	8.939~ 9.522(um)	31.5~ 33.6 (THz)	~	~	0.212	Shin-Tson Wu, Physical Review A, Vol 33, Number 2 (1986)
Intermediate IR	5.539~ 5.884(um)	51~ 54.2 (THz)	~	~	0.181	Shin-Tson Wu, Physical Review A, Vol 33, Number 2 (1986)
	3.628~ 4.317(um)	69.5~ 82.7 (THz)	~	~	0.192	Shin-Tson Wu, Physical Review A, Vol 33, Number 2 (1986)
	3.511~ 3.993(um)	75.13~ 85.45 (THz)	~	~	0.145	N. J. DIORIO JR, Liquid Crystals, Vol. 29, No. 4, 589-596
	2.513~ 3.364(um)	89.18~ 119.4 (THz)	~	~	0.158	N. J. DIORIO JR, Liquid Crystals, Vol. 29, No. 4, 589-596
Near IR	1.611~ 2.833(um)	106~ 186 (THz)	~	~	0.191	Shin-Tson Wu, Physical Review A, Vol 33, Number 2 (1986)
	1.55 (um)	193.5 (THz)	1.693	1.507	0.186	Shin-Tson Wu, Journal of Applied Physics 97, 073501 (2005)
	1.55 (um)	193.5 (THz)	1.684	1.500	0.183	S. Brugioni, Infrared physics & Technology 49, 210-212 (2007)
Visible	656(nm)	457 (THz)	1.726	1.518	0.208	Jun Li, Shin-Tson Wu, IEEE/OSA Journal of display technology, Vol. 1, No. 1(2005)
	633(nm)	474 (THz)	1.731	1.519	0.212	Jun Li, Shin-Tson Wu, IEEE/OSA Journal of display technology, Vol. 1, No. 1(2005)

Visible	633(nm)	474 (THz)	~	~	0.22	Shin-Tson Wu, Physical Review A, Vol 33, Number 2 (1986)
	589 (nm)	509 (THz)	1.74	1.52	0.22	Shin-Tson Wu, Journal of Applied Physics 97, 073501 (2005)
	589 (nm)	509 (THz)	1.739	1.523	0.216	Jun Li, Shin-Tson Wu, IEEE/OSA Journal of display technology, Vol. 1, No. 1(2005)
	546 (nm)	549 (THz)	1.751	1.527	0.224	Jun Li, Shin-Tson Wu, IEEE/OSA Journal of display technology, Vol. 1, No. 1(2005)
	486 (nm)	617 (THz)	1.776	1.535	0.241	Jun Li, Shin-Tson Wu, IEEE/OSA Journal of display technology, Vol. 1, No. 1(2005)
	450 (nm)	667 (THz)	1.801	1.542	0.259	Jun Li, Shin-Tson Wu, IEEE/OSA Journal of display technology, Vol. 1, No. 1(2005)

3.2 Determination of optical constants

For the purpose of deriving the complex optical constants without Kramers-Kronig relation, the field amplitude and phase of THz wave transmitted through the reference and the LC cell were used.

Assuming THz wave is a plane wave passing through the cells from one side to another side, and the electric field of the THz goes through the reference cell was given by,

$$E_{reference}(\tau)=\int_{-\infty}^{\infty}E_i(\nu)\tilde{t}_{aw}\tilde{t}_{wa}\exp\left\{i2\pi\nu\left[\frac{\tilde{n}_w(d_1+d_2)}{c}\right]\right\}\exp\left\{i2\pi\nu\left[\frac{\tilde{n}_a(d_a+\Delta d)}{c}\right]\right\}\exp\left(i2\pi\nu\tau\right)d\nu \tag{3.1}$$

where $E_i(\nu)$ is the original THz wave which has not passed through the cell yet.

$\tilde{t}_{aw}=2\tilde{n}_a/(\tilde{n}_a+\tilde{n}_w)$ and $\tilde{t}_{wa}=2\tilde{n}_w/(\tilde{n}_w+\tilde{n}_a)$ are the transmission coefficient from air to a fused silica

substrate and from substrate to air, respectively. $\tilde{n}_w$ and $\tilde{n}_a$ are the refractive index of substrate and air. Similarly, the electric field of the THz wave passed through the LC can be represented as,

$$E_{LC}(\tau)=\int_{-\infty}^{\infty}E_i(\nu)\tilde{t}_{aw}\tilde{t}_{w-LC}\tilde{t}_{LC-w}\tilde{t}_{wa}\exp\left\{i2\pi\nu\left[\frac{\tilde{n}_w(d_3+d_4)}{c}\right]\right\}\cdot\sum_{m=0}^{N}\left[\tilde{r}_{LC-w}^{2m}\times\exp\left\{i2\pi\nu\left[\frac{\tilde{n}_{LC}d_{LC}}{c}(2m+1)\right]\right\}\right]\cdot\exp\left(-i2\pi\nu\tau\right)d\nu \tag{3.2}$$

where $\tilde{t}_{w-LC}=2\tilde{n}_w/(\tilde{n}_w+\tilde{n}_{LC})$ and $\tilde{t}_{LC-w}=2\tilde{n}_{LC}/(\tilde{n}_{LC}+\tilde{n}_w)$ are the transmission coefficient from

fused silica substrate to the LC cell and from LC cell to the substrate interfaces, respectively.

$\sum_{m=0}^{N}\left(\tilde{r}_{LC-w}^{2m}\times\exp\left\{i2\pi\nu\left[\frac{\tilde{n}_{LC}d_{LC}}{c}(2m+1)\right]\right\}\right)$ means the Fabry-Perot coefficient in the

nematic LC cell with a thickness of d_{LC}, and $\tilde{n}_{LC}$ is the complex refractive index of LC.

Here, the difference of d_1+d_2 and d_3+d_4 is considered as Δd so that we can reduce

the error of thickness.

Because of **Eq. (3.1)** and **Eq. (3.2)**, we can represent the transmission coefficient **Eq. (3.3)**,

$$\left[T(\nu)\right]^{1/2}\times\exp\left[i(\phi_{LC}-\phi_{reference})\right]=\frac{E_{LC}(\nu)}{E_{reference}(\nu)}=\left[\frac{4\cdot\tilde{n}_{LC}\cdot\tilde{n}_w}{(\tilde{n}_{LC}+\tilde{n}_w)^2}\cdot F_{LC}(\nu,d_{LC})\cdot\exp\left\{\frac{i2\pi\nu}{c}\left[d_{LC}(\tilde{n}_{LC}-\tilde{n}_a)+\Delta d(\tilde{n}_w-\tilde{n}_a)\right]\right\}\right] \tag{3.3}$$

where the **Eq. (3.3)** includes the information of power transmittance and phase shift [**19**], and we can use them to derive the complex refractive index as follows,

$$n_{LC}=\frac{1}{2\pi\nu\frac{d_{LC}}{c}}\left((\phi_{LC}-\phi_{reference})-\arg\left[\tilde{t}_{w-LC}\tilde{t}_{LC-w}\sum_{m=0}^{N}\left(\tilde{r}_{LC-w}e^{i2\pi\nu(\frac{\tilde{n}_{LC}d_{LC}}{c})}\right)^{2m}\right]\exp\left\{\frac{-2\pi\nu}{c}\left[(\kappa_{LC}-\kappa_a)d_{LC}+(\kappa_w-\kappa_a)\Delta d\right]\right\}\right)+n_a-\frac{(n_w-n_a)\Delta d}{d_{LC}}$$

(3.4)

$$\kappa_{LC}=\kappa_a+\frac{(\kappa_w-\kappa_a)\Delta d}{d_{LC}}+\frac{c}{-2\pi\nu d_{LC}}\ln\left(\frac{\left(\frac{T_{LC}}{T_{reference}}\right)^{1/2}}{\left|\tilde{t}_{w-LC}\tilde{t}_{LC-w}\sum_{m=0}^{N}\left\{\tilde{r}_{LC-w}\exp\left[i2\pi\nu(\frac{\tilde{n}_{LC}d_{LC}}{c})\right]\right\}^{2m}\exp\left\{\frac{-2\pi\nu}{c}\left[(\kappa_{LC}-\kappa_a)d_{LC}+(\kappa_w-\kappa_a)\Delta d\right]\right\}\right|}\right)$$

(3.5)

The symbols we used before were shown as **Fig. 3.1**. Since a nematic LC can be viewed as a uniaxial crystal, the n_e and n_o of LC can be obtained by rotating the cell to adjust the director being perpendicular or parallel to the polarization direction of THz wave, respectively.

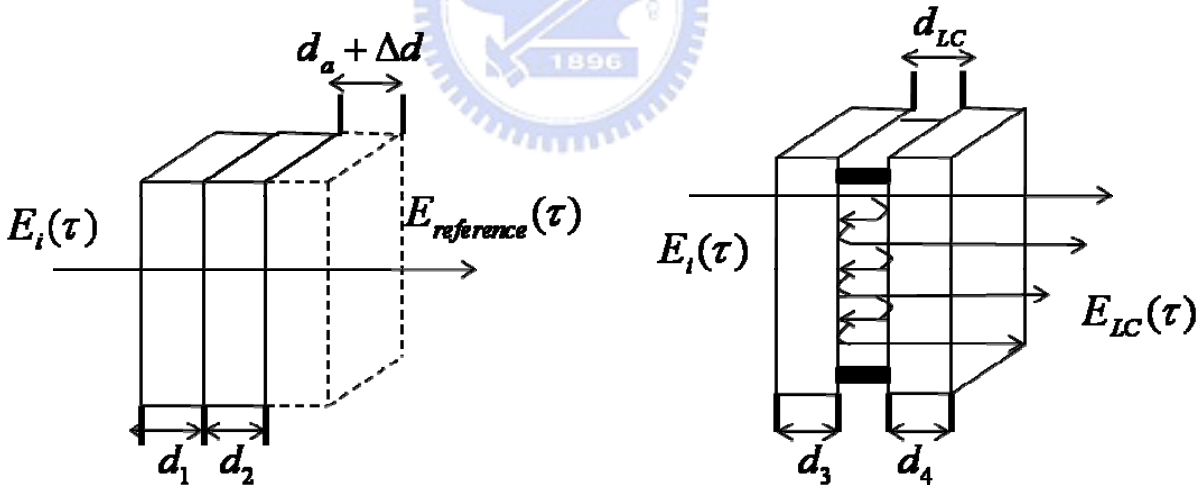

Fig. 3.1 The symbols of deriving the complex refractive index

3.3 A Model Describing the Temperature Effect of LC Refractive Indices

The origin Cauchy equation, which has been used to fitting the refractive indices of anisotropic liquid crystals [**57**], but the physical meaning of fitting results is not clear exactly. Before determining how the properties of LCs are related to the susceptibility, we have to figure out the differences between the fields acting on the molecules in the medium and the applied field.

3.3-1 Effective Medium Theory

3.3-1-1 Depolarization Field

The charges bound in each molecule will respond to the applied field if an electric field is applied to a medium made up of a large number of molecules [**58**]. Therefore, there is produced in the medium an electric polarization ($\vec{P}$, dipole moment per unit volume) given by:

$$\vec{P}(x) = \sum_i N_i < \vec{p}_i > \tag{3.6}$$

Here, $\vec{p}_i$ is the dipole moment of the *i*th type of molecule in the medium, the average is take over a small volume centered at x. The N_i is the average number per unit volume of the *i*th type of molecule at the point x.

For macroscopic field, the total field comes from the applied field ($\vec{E}_0$) and induced average polarization ($\vec{E}_P$) which is the field due to the uniform polarization and opposing the $\vec{E}_0$ [**59**]. The relationship between them is shown as **Fig 3.2**.

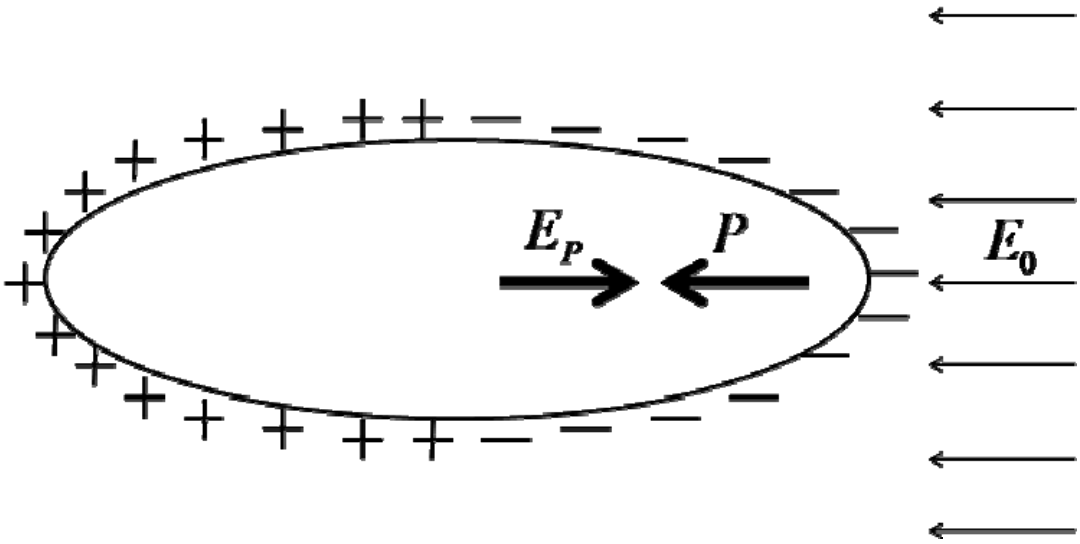

Fig 3.2 The depolarization field E_P is opposite to P. The fictitious surface charges are indicate. The field of these charges is E_P within the ellipsoid.

We can determine the components of the depolarization field as Eq. 3.7 if P_x, P_y, P_z are the principal axes of an ellipsoid of P.

$$E_{Px} = -N_x P_x;\ \ E_{Py} = -N_y P_y;\ \ E_{Pz} = -N_z P_z \tag{3.7}$$

Where N_x, N_y, N_z are the depolarization factors depending on the ratios of principal axes.

The uniform polarization in an ellipsoid will be induced by a uniform applied field $\vec{E}_0$. By the relation of $\vec{P} = \chi_e \vec{E}$ and $E = E_0 + E_P = E_0 - NP$, we can describe the macroscopic field as **Eq. (3.8)**.

$$P = \chi_e (E_0 - NP) \tag{3.8}$$

Where χ_e is dielectric susceptibility.

3.3-1-2 Lacal Electric Field of Single Atom

The local electric field of single atom which is significantly different from the macroscopic electric field can be described as **Eq. (3.9)** [**59**].

$$\vec{E}_{local} = \vec{E}_0 + \vec{E}_P + \vec{E}_L + \vec{E}_{near} \tag{3.9}$$

Where $\vec{E}_0$ is field produced by fixed charges external to the body, $\vec{E}_P$ is depolarization

field, $\vec{E}_L$ is Lorentz cavity field which comes from polarization charges on inside of a spherical cavity, and the $\vec{E}_{near}$ is the field of atoms inside cavity. These components are shown as **Fig 3.3**.

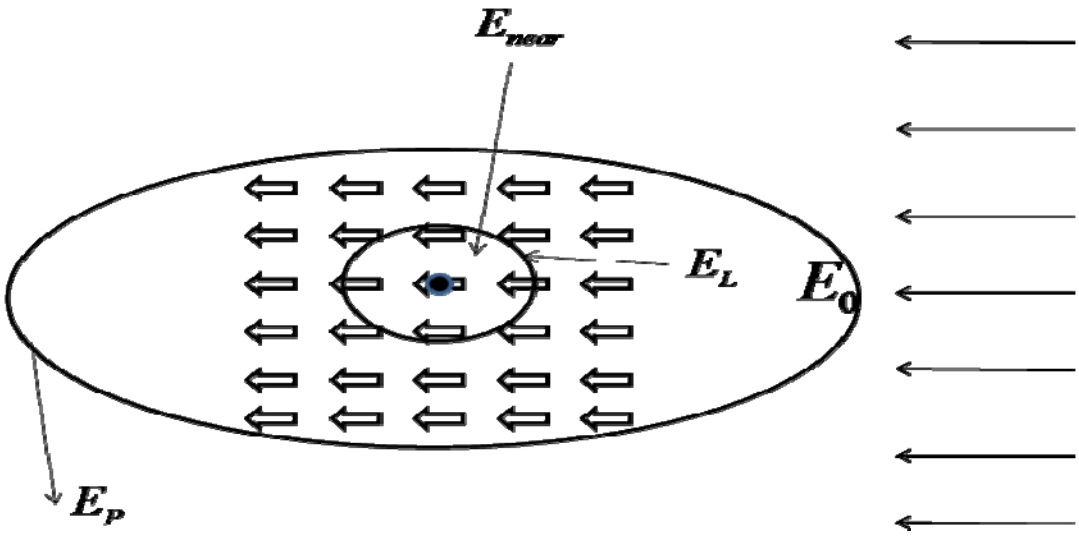

Fig 3.3 The internal electric field on an atom in a crystal is the sum of the external applied field $\vec{E}_0$ and of the field due to the other atoms in the crystal.

3.3-1-3 Lorentz Field

We consider the filed $\vec{E}_L$ induced by the polarization charges on the surface of the fictitious cavity [**59**]. The figure of calculation of the field in a spherical cavity in a uniform polarized medium is shown as **Fig 3.4**:

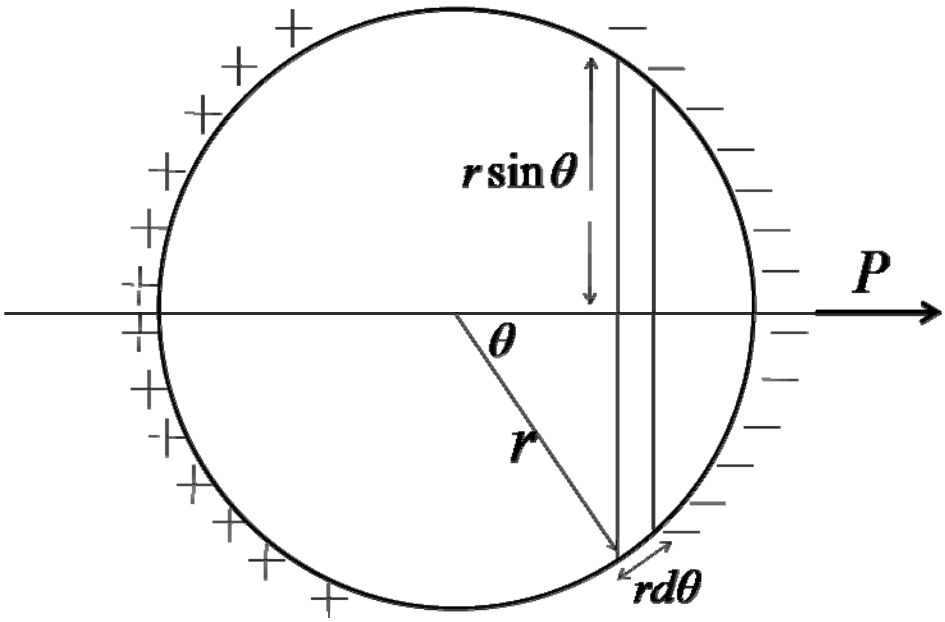

Fig 3.4 Estimation of the field in a spherical fiction in a uniformly polarized medium.

We can describe the electric field at the center is

$$\vec{E}_L = \int_0^{\pi} (2\pi r \sin\theta)\cdot(rd\theta)\cdot(P\cos\theta)\cdot\cos\theta / a^2 = \frac{4\pi}{3}P \qquad (3.10)$$

Here, the θ is the polar angle with polarization direction, the surface charge density is $-P\cos\theta$, and the charges on ring are $2\pi r\sin\theta\cdot rd\theta\cdot P\cos\theta$.

3.3-1-4 Dielectric Constant and Polarizability

Above of all, the total field can be written as **Eq. (3.11)**:

$$\vec{E}_{local} = \vec{E}_0 + \vec{E}_P + \vec{E}_L + \vec{E}_{near} = \vec{E} + \frac{4\pi}{3}\vec{P} \qquad (3.11)$$

Here, $\vec{E}_0 + \vec{E}_P$ can be written as $\vec{E}$ in the assumption of macroscopic field, and $\vec{E}_{near}$ vanishes for a highly symmetric situation.

On the other hand, the polarization vector $\vec{P}$ can be defined in **Eq. (3.12)** as

$$\vec{P} = N < \vec{p}_{mol} > \qquad (3.12)$$

Here, the $< \vec{p}_{mol} >$ is the average dipole moment of the molecules, and the molecular

polarizability (α) is also defined as **Eq. (3.13)** in order to exhibit this dependence on electric field.

$$< \vec{p}_{mol} >= \alpha \vec{E} \tag{3.13}$$

Eq. (3.12) can be combined with **Eq. (3.11)** and **Eq. (3.13)**, and we show that as **Eq. (3.14)**:

$$\vec{P} = N\alpha(\vec{E} + \frac{4\pi}{3}\vec{P}) \tag{3.14}$$

We solve for $\vec{P}$ in terms of $\vec{E}$, and use the definition of electric susceptibility $\vec{P} = \chi_e \vec{E}$, we can realize the susceptibility:

$$\chi_e = \frac{\vec{P}}{\vec{E}} = \frac{N\alpha}{1 - \frac{4\pi}{3}N\alpha} \quad \text{.....} \quad \text{.....} \quad \text{.....} \tag{3.15}$$

Since the dielectric constant is $\varepsilon_r = 1 + 4\pi\chi_e$, we can express the molecular polarizability in terms of dielectric constant:

$$\alpha = \frac{3}{4\pi N}\frac{\varepsilon_r - 1}{\varepsilon_r + 2} \tag{3.16}$$

The **Eq. (3.16)** is called Clausius-Mossotti equation, and the main principle of Clausius-Mossotti equation focuses on any $\varepsilon_r - 1/\varepsilon_r + 2$ should be proportional to the material; density [**58**].

3.3-2 Extended Cauchy Equations

From the Clausius-Mossotti equation shown as **Eq. (3.16)** and $\varepsilon_r = n^2$, we can obtain the Lorentz-Lorenz equation [**58**]:

$$\frac{n^2 - 1}{n^2 + 2} = \frac{4\pi}{3}N\alpha \tag{3.17}$$

In fact, the equation is not suitable for anisotropic LCs which demonstrate the birefringence (n_e, n_o), molecular polarizabilities (α_e, α_o) and dielectric constants ($\varepsilon_e, \varepsilon_o$). In order to consider the anisotropic condition, an assumption **Eq. (3.18)** made by Vuks describes the

internal field in a crystal is the same in every direction [**60**].

$$E_i = \frac{<n^2>+2}{3}E \tag{3.18}$$

Here, E_i is the uniformly internal field which acts on a molecule, and E is the macroscopic electric field.

We can derive **Eq. (3.19)** by replacing the n^2 in the denominator of **Eq. (3.17)** by $<n^2>=(n_e^2+2n_o^2)/3$, the n^2 in the numerator by $n_{e,o}^2$ and the α is also replaced by $\alpha_{e,o}$ [**61**].

$$\frac{n_{e,o}^2-1}{<n^2>+2} = \frac{4\pi}{3}N\alpha_{e,o} \tag{3.19}$$

Where $<n^2>$ is defined as **Eq. (3.20)**:

$$<n^2>=(n_e^2+2n_o^2)/3 \tag{3.20}$$

We substituting **Eq. (3.20)** into **Eq. (3.19)**, and we can obtain

$$n_e = [1+\frac{4\pi N\alpha_e}{1-\frac{4}{3}\pi N<\alpha>}]^{1/2} \tag{3.21}$$

$$n_o = [1+\frac{4\pi N\alpha_o}{1-\frac{4}{3}\pi N<\alpha>}]^{1/2} \tag{3.22}$$

Here, $<\alpha>$ defined as **Eq. (3. 23)** is the average polarizability of the LC molecule [**62**].

$$<\alpha>=\frac{\alpha_e+2\alpha_o}{3} \tag{3.23}$$

Assume the $N<\alpha>$ is insignificant, so the **Eq. (3.21)** and **(3.22)** can be expanded into a power series. Rearrange these term, we can derive

$$n_e \approx \frac{3\sqrt{2}}{4}+\frac{\sqrt{2}\pi N<\alpha>}{1-\frac{4}{3}\pi N<\alpha>}+\frac{(2\sqrt{2}/3)\pi NS(\gamma_e-\gamma_o)}{1-\frac{4}{3}\pi N<\alpha>} \tag{3.24}$$

$$n_o \approx \frac{3\sqrt{2}}{4} + \frac{\sqrt{2}\pi N < \alpha >}{1 - \frac{4}{3}\pi N < \alpha >} - \frac{\sqrt{2}/3\pi NS(\gamma_e - \gamma_o)}{1 - \frac{4}{3}\pi N < \alpha >} \tag{3.25}$$

Where S is the order parameter and $\gamma_e - \gamma_o$ is the differential molecular polarizability in the crystalline state [**63**].

The average refractive indices is described as **Eq. (3.26)**:

$$< n >= \frac{n_e + 2n_o}{3} \tag{3.26}$$

We substitute the **Eq. (3.24)** and **Eq. (3.25)** into **Eq. (3.26)**, and we can obtain:

$$< n >\approx \frac{3\sqrt{2}}{4} + \frac{\sqrt{2}\pi N < \alpha >}{1 - \frac{4}{3}\pi N < \alpha >} \tag{3.27}$$

By subtracting **Eq. (3.25)** from **Eq. (3.24)**, we can derive the birefringence ($\Delta n = n_e - n_o$) of LC which is shown as **Eq. (3.28)**:

$$\Delta n \approx \frac{\sqrt{2}\pi NS(\gamma_e - \gamma_o)}{1 - \frac{4}{3}\pi N < \alpha >} \tag{3.28}$$

We have the simple expressions shown as **Eq. (3.29)** and **Eq. (3.30)** of refractive indices by substituting **Eq. (3.26)** and **Eq. (3.28)** into **Eq. (3.24)** and **Eq. (3.25)** [**62**].

$$n_e =< n > + \frac{2}{3}\Delta n \tag{3.29}$$

$$n_o =< n > - \frac{1}{3}\Delta n \tag{3.30}$$

From our experimental data and fitting condition, $< n >$ decreases when the temperature increases:

$$< n(T) >= A - BT \tag{3.31}$$

Furthermore, the birefringence (Δn) shown as **Eq. (3.32)** is dependent on the order parameter approximated as $S = (1 - T / T_c)^{\beta}$.

$$\Delta n(T) = (\Delta n)_o (1 - T / T_c)^{\beta} \tag{3.32}$$

Here, the slope of **Eq. (3.31)** is negative, and the value of B is in the order of 10^{-4} (K^{-1}). On the other hand, $(\Delta n)_0$ is the birefringence in the crystalline state, the β is a material constant, and T_c is the clearing temperature of the LC we used [**62**].

Above of all, we can substitute **Eq. (3.31)** and **Eq. (3.32)** into **Eq. (3.29)** and **Eq. (3.30)**, and we can derive the four-parameter model shown as **Eq. (3.33)** and **Eq. (3.34)**:

$$n_e(T) \approx A - BT + \frac{2(\Delta n)_0}{3}(1 - \frac{T}{T_c})^{\beta} \tag{3.33}$$

$$n_o(T) \approx A - BT - \frac{(\Delta n)_0}{3}(1 - \frac{T}{T_c})^{\beta} \tag{3.34}$$

All of these fitting parameters can be obtained directly by fitting the temperature-dependent $<n>$ and Δn, respectively.

Chapter 4 Results and Discussions

4.1 Complex optical constants

Figure 4.1 shows an example of the measured time-domain waveform of the THz signal that transmitted through the reference and LC cells at 26 ºC for e-ray and o-ray. The corresponding amplitude and the phase spectra, shown in **Fig. 4.2**, are obtained by applying a fast Fourier transform (FFT) to the time-domain waveforms. The time delay of signal passing through the LC cell with respect to that of the reference is evident in **Fig. 4.1**. The optical constants of the LC are then determined using the procedure described in the previous section.

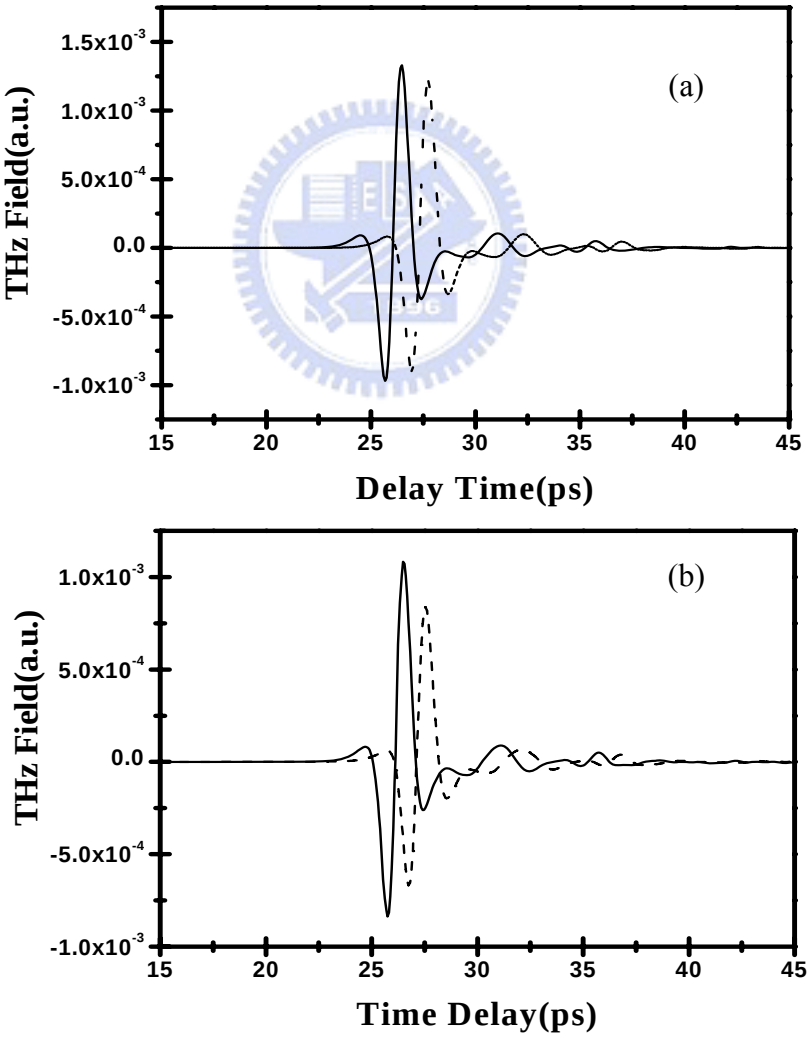

Fig. 4.1. Transmitted THz signals (*e* ray) through the reference (solid line) and LC cell (dashed line) at 26°C for (a) e-ray and (b) o-ray.

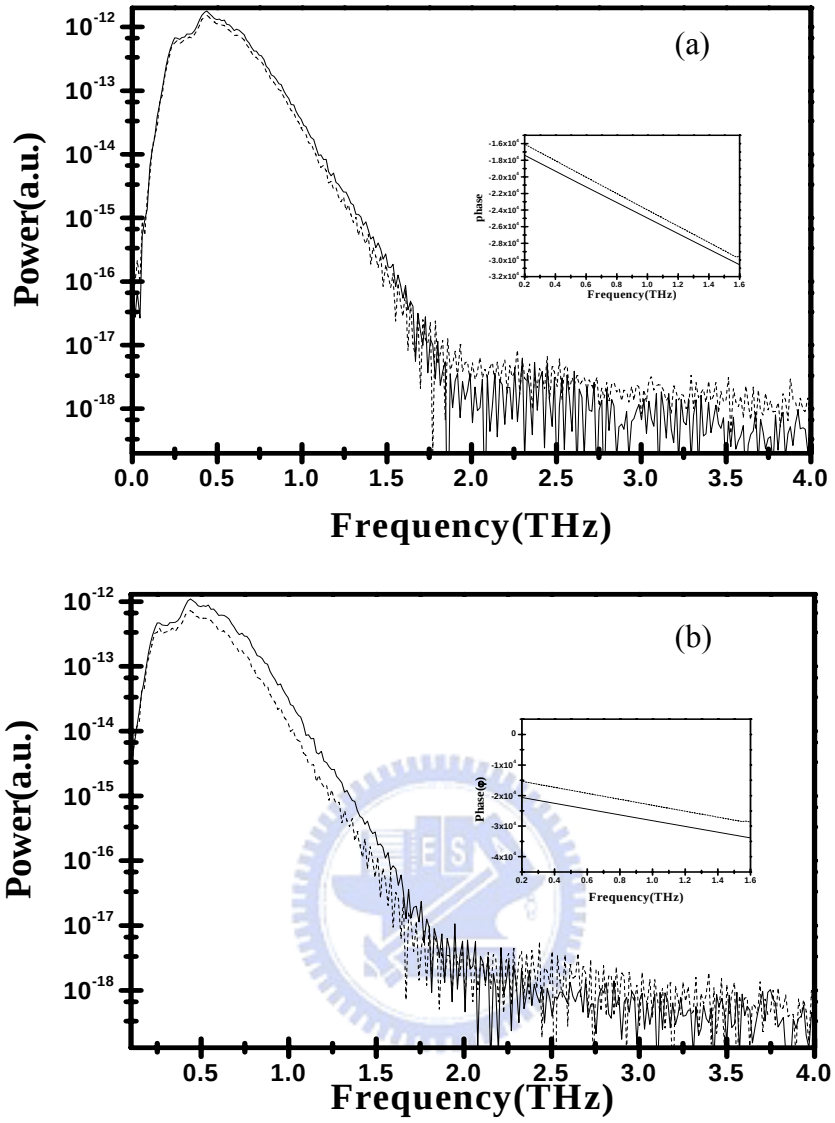

Fig. 4.2. Power spectra of the transmitted THz signals (*e* ray) through the reference (solid line) and LC cell (dashed line) at 26°C for (a) o-ray and (b) e-ray. The insets are the corresponding phase spectra.

In the frequency range of 0.2~1.4 THz, the real part of optical constants of E7 at 26°C are shown as a function of frequency in **Fig. 4.3**. The blue circles and red triangles are the extraordinary and ordinary indices, n_e, n_o, respectively. Clear anisotropy was observed, with n_e = 1.71 ± 0.01, n_o = 1.57 ± 0.02. The room-temperature birefringence of E7 in the THz frequency range is thus 0.14± 0.03. 1.609 + 0.009i 1.761 + 0.006i 0.152. The real index of

refraction of E7 in the isotropic phase, n_{iso} = 1.61 ± 0.01. 1.61 ± 0.01 was measured at 59°C. As expected, n_{iso} of E7 fall between ne and no, and are given approximately by n_{iso} = $(2n_e+n_o)/3$. On the other hand, for the imaginary part of the refractive indices (κ), we note that κ_e = 0.014 ± 0.002, κ_o = 0.036 ± 0.004 and κ in the isotropic phase is 0.030 ± 0.005. All of them are smaller than 0.040 in the frequency range, and κ_o is almost higher than κ_e in 0.022 ± 0.002. These data are shown as **Fig. 4.4**.

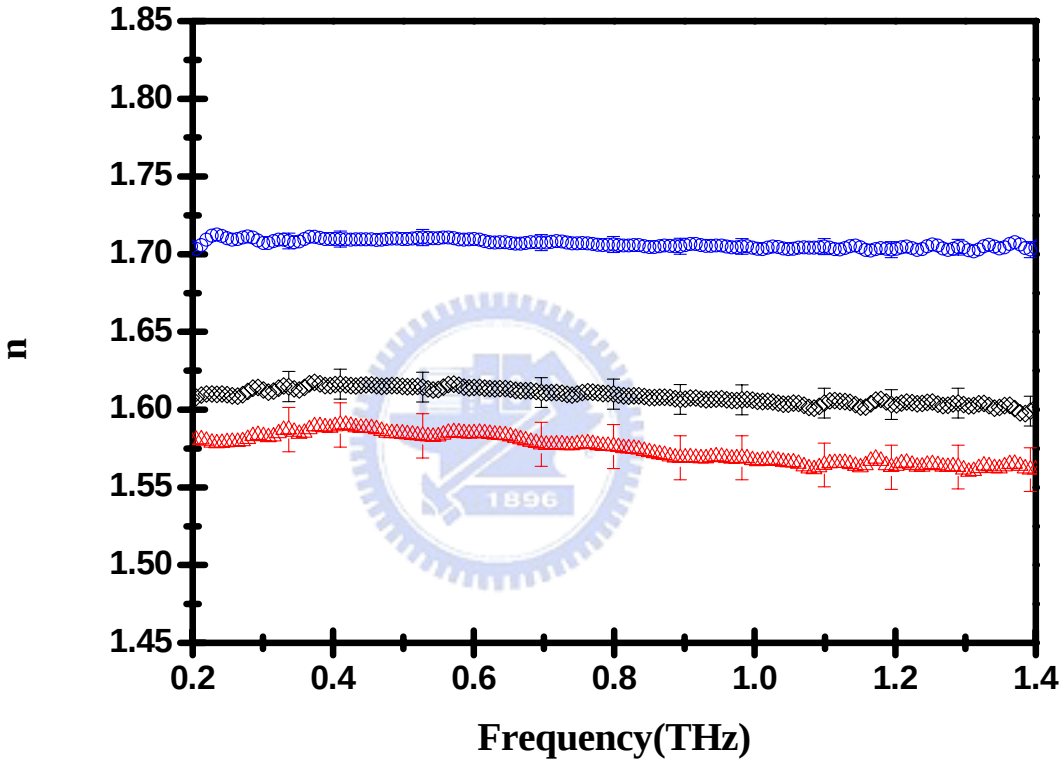

Fig. 4.3. The real refractive indices of E7 are plotted as fuctions of frequency. The blue circles and the red triangles are the n_e and n_o at 26°C, respectively.The black diamonds are the real indices of isotropic phase.

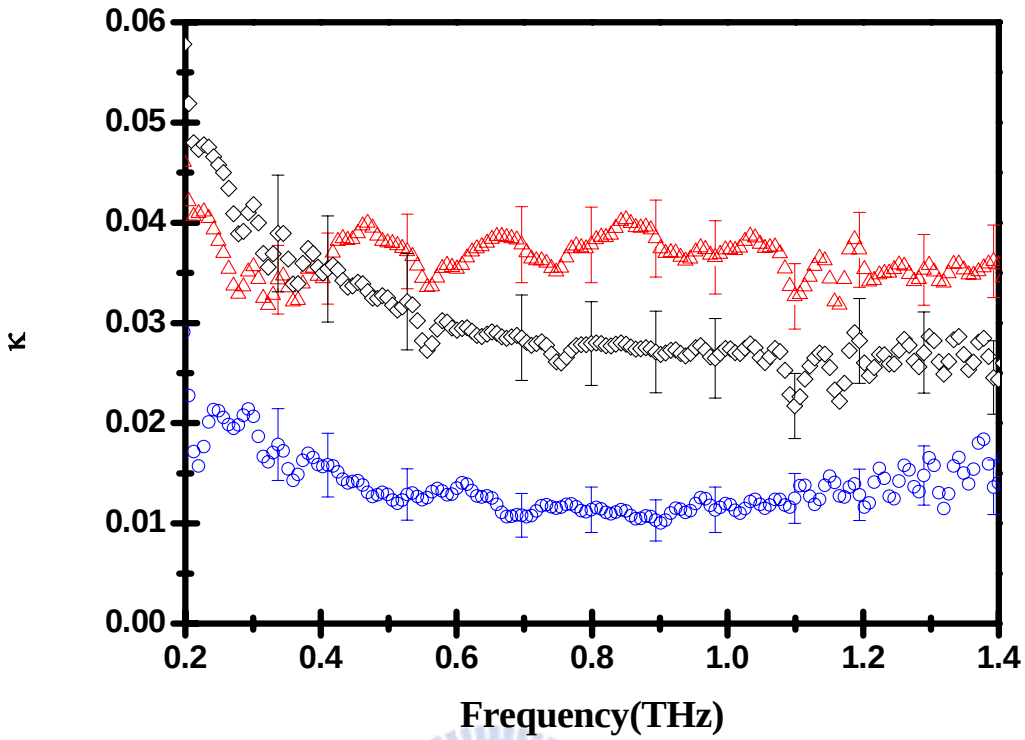

Fig. 4.4. The imaginary refractive indices of E7 are plotted as functions of frequency. The blue circles and the red triangles are the κ_e and κ_o at 26°C, respectively.The black diamonds are the imaginary indices of isotropic phase.

When calculating the complex refractive indices, we have to check the complex refractive indices of the substrate composed of fused silica. We apply the same way of Chapter. 3.2, and the results are shown as **Fig. 4.5 (a)** and **Fig. 4.5 (b)**, respectively. The real refractive indices of fused silica are approximately 1.95 from 0.2 THz to 1.4 THz, and the imaginary indices (κ) are almost smaller than 0.01.

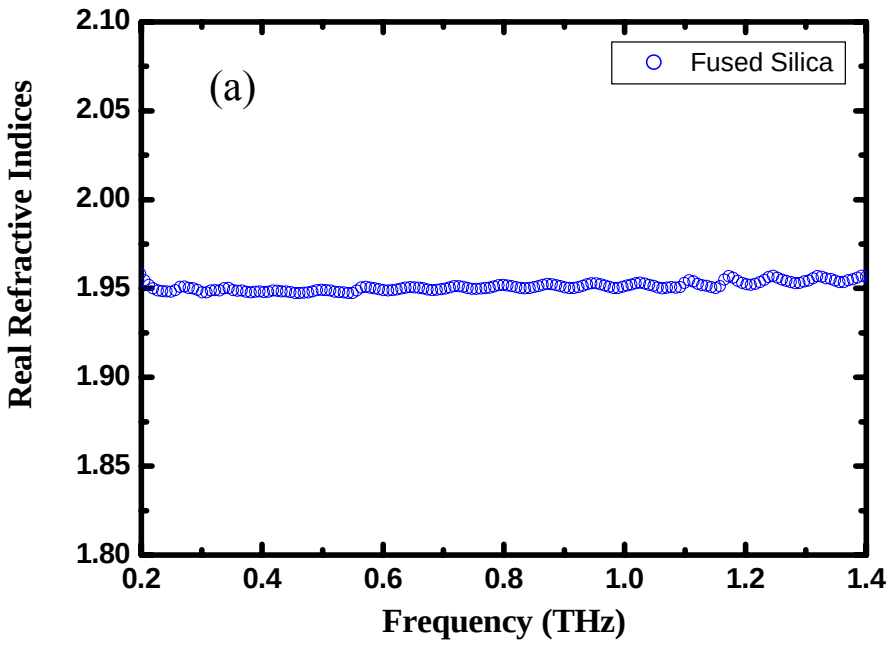

Fig. 4.5 (a) The real refractive indices of fused silica are plotted as fuctions of frequency at 26°C.

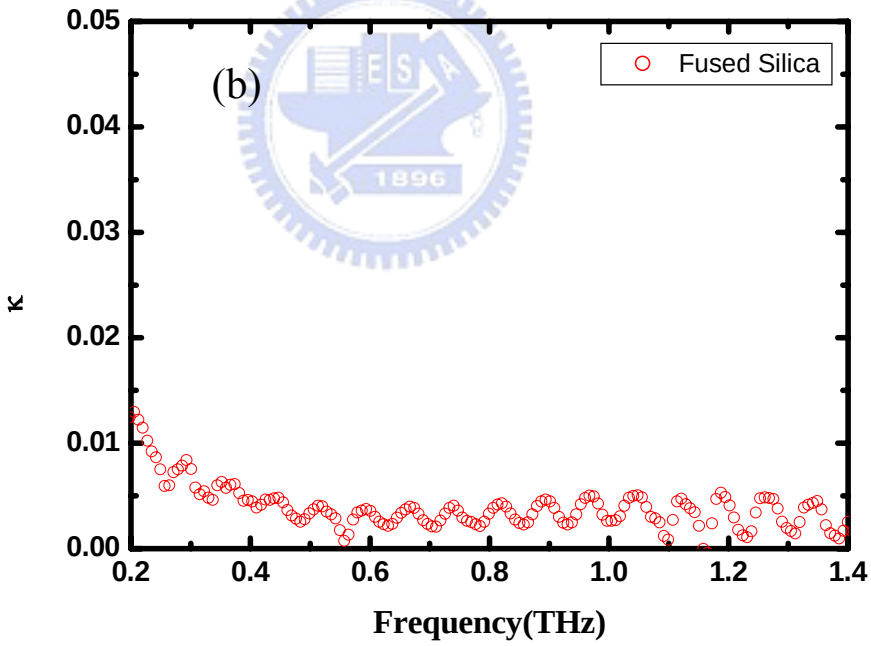

Fig. 4.5 (b) The imaginary refractive indices of E7 are plotted as functions of frequency at 26°C.

4.2 Temperature dependence of refractive indices

The effect of temperature plays an very important role on the refractive indices of LC. Most of all, n_e shows the different behavior from n_o as the temperature increases. Temperature gradient of n_e (dn_e / dT) is negative for most of LCs material, but the temperature gradient of n_o (dn_o / dT) can change from negative to positive because of operating temperature and material of LCs [**64**]. In order to modulate the temperature of LC devices, the temperature dependence of refractive indices is needed accurately.

4.2-1 Temperature Effect on Real Refractive Indices

We show the real refractive indices of temperature dependence of E7 at 0.34, 0.41, 0.53, 0.70, 0.80, 0.89, 0.98, 1.10, 1.19, 1.29, 1.39 THz as **Fig. 4.6 (a) and (b)**, in which the open circles and open triangles are the real refractive indices of n_e and n_o, respectively. From **Eq. (3.33)** and **Eq. (3.34)**:

$$n_e(T) \approx A - BT + \frac{2(\Delta n)_0}{3}(1-\frac{T}{T_c})^{\beta} \tag{3.33}$$

$$n_o(T) \approx A - BT - \frac{(\Delta n)_0}{3}(1-\frac{T}{T_c})^{\beta} \tag{3.34}$$

We can fit the real refractive indices of temperature dependence of E7 directly, and these fitting parameters (A, B, $(\Delta n)_0$ and β) which shown as **Table 4.1** can be obtained at the same time.

However, A, B, $(\Delta n)_0$ and β can also be checked by the two-step fittings. The first step is to derive the average refractive indices ($< n >= \frac{n_e + 2n_o}{3}$) and obtain parameters (A, B) by the **Eq. (3.31)**. Another step is to use **Eq. (3.32)** to fit the data of birefringence so that

we can get the information of $(\Delta n)_0$ and β. Later, we will show the results of the two-step fittings exactly.

Table. 4.1 The fitting parameters of Eq. (3.33) and (3.34) for frequencies from 0.34 to 1.40 THz.

THz	$A(n_e)$	$A(n_o)$	$B(n_e)$	$B(n_o)$	$(\Delta n)_0(n_e)$	$(\Delta n)_0(n_o)$	$\beta(n_e)$	$\beta(n_o)$
0.34	1.6600	1.6680	2.29×10^{-4}	1.51×10^{-4}	0.3050	0.2000	0.2272	0.2098
0.41	1.6600	1.6681	2.25×10^{-4}	1.49×10^{-4}	0.2993	0.2000	0.2196	0.2274
0.53	1.6600	1.6672	2.26×10^{-4}	1.53×10^{-4}	0.3047	0.2000	0.2223	0.2146
0.70	1.6600	1.6691	2.26×10^{-4}	1.54×10^{-4}	0.2947	0.2188	0.2209	0.1900
0.80	1.6600	1.6681	2.24×10^{-4}	1.57×10^{-4}	0.2848	0.2181	0.2134	0.1900
0.89	1.6600	1.6666	2.26×10^{-4}	1.60×10^{-4}	0.2867	0.2402	0.2179	0.1900
0.98	1.6600	1.6655	2.24×10^{-4}	1.62×10^{-4}	0.2795	0.2323	0.2098	0.1900
1.10	1.6600	1.6639	2.19×10^{-4}	1.65×10^{-4}	0.2796	0.2448	0.2120	0.1900
1.19	1.6600	1.6663	2.16×10^{-4}	1.61×10^{-4}	0.2730	0.2664	0.2132	0.1900
1.29	1.6600	1.6680	2.11×10^{-4}	1.58×10^{-4}	0.2729	0.2772	0.2110	0.1900
1.40	1.6600	1.6626	2.24×10^{-4}	1.67×10^{-4}	0.2875	0.2491	0.2269	0.1900

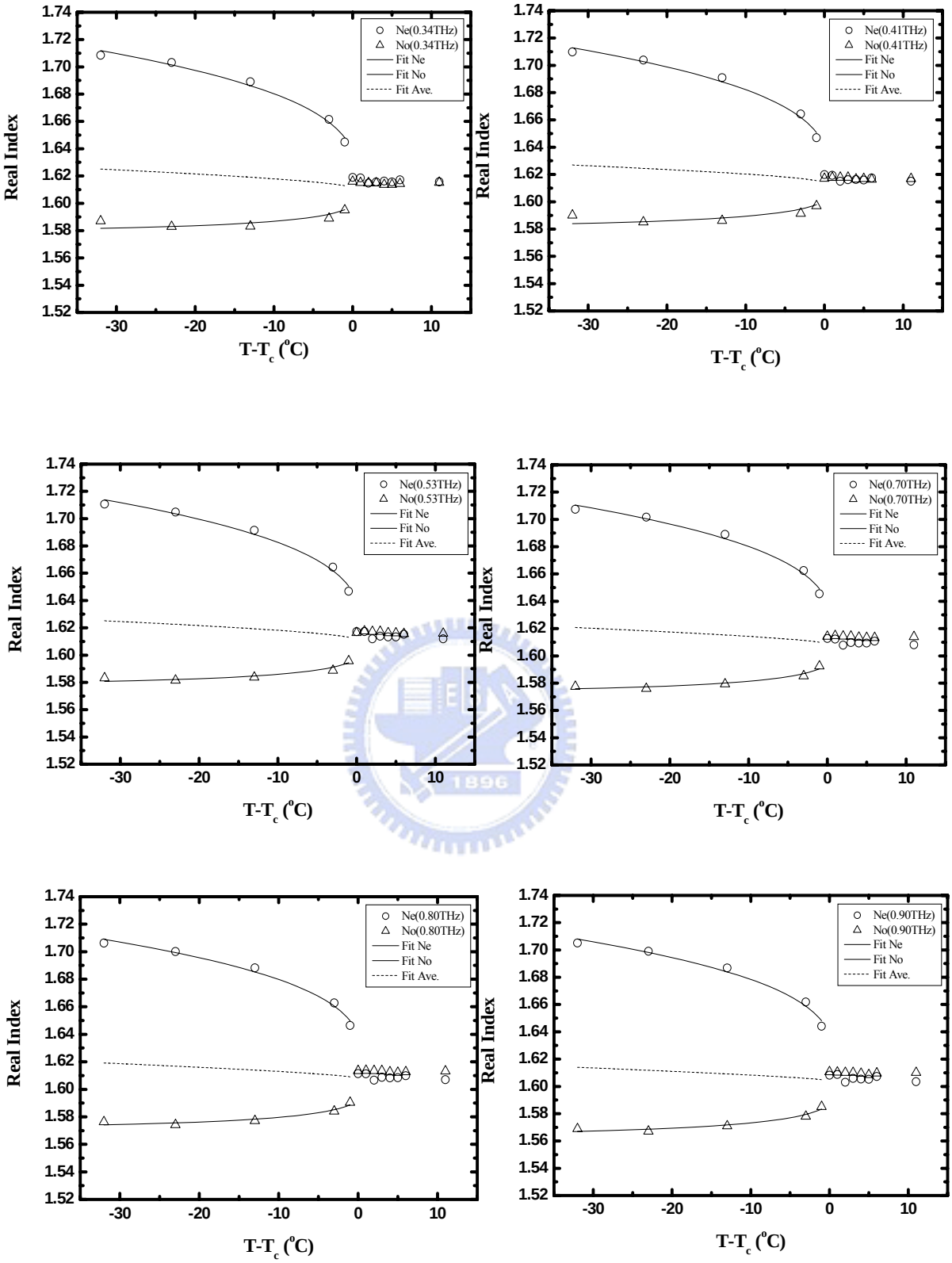

Fig. 4.6 (a) Extraodinary and ordinary refractive indices of E7 are plotted as functions of reduced temperature at frequency of 0.34, 0.41, 0.53, 0.709, 0.80 and 0.90 THz. The open circles and the open triangles represent n_e and n_o, respectively. The dash lines are the average index, $(2 \cdot n_o + n_e)/3$ at temperatures below T_c.

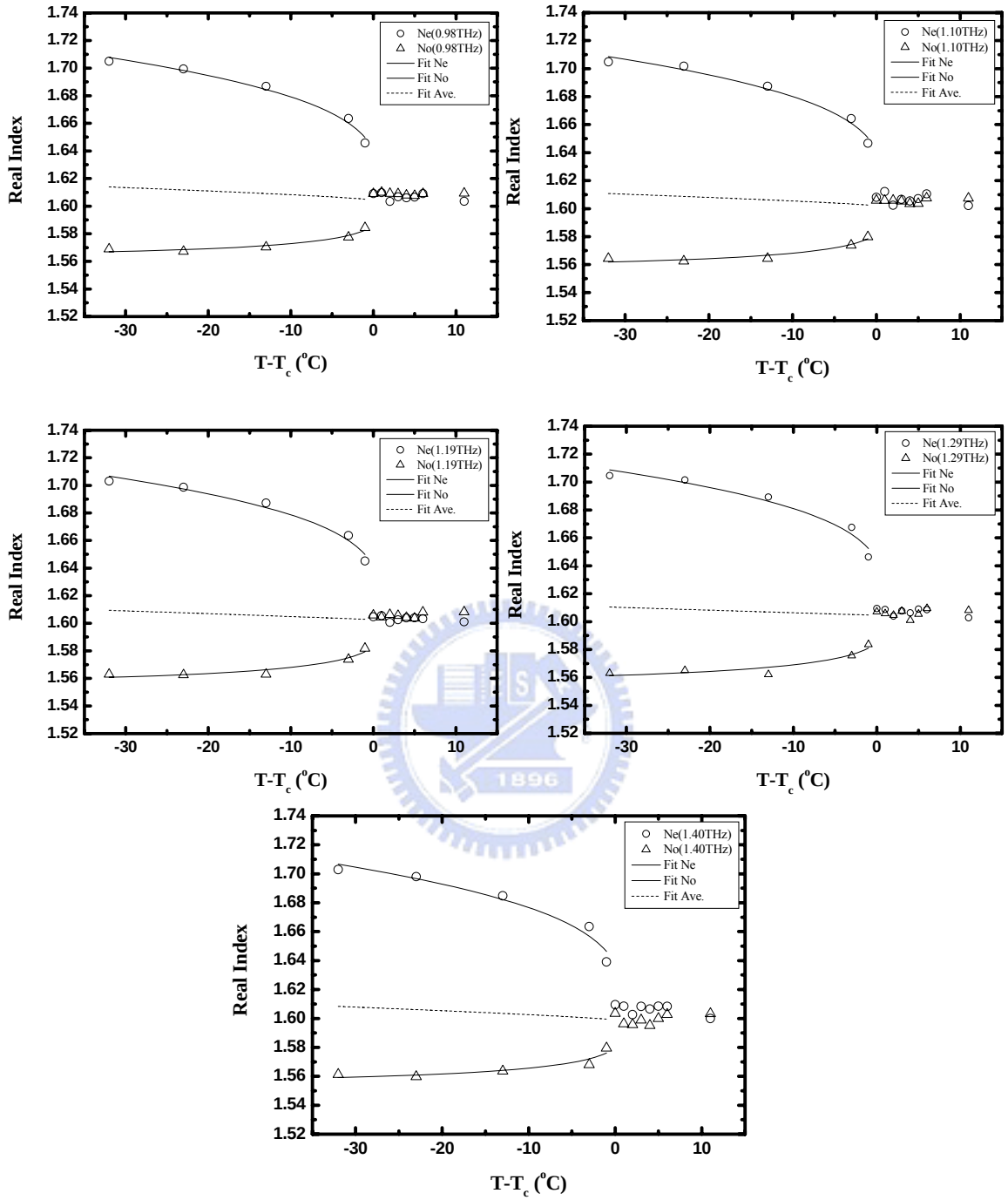

Fig. 4.6 (b) Extraodinary and ordinary refractive indices of E7 are plotted as functions of reduced temperature at frequency of 0.98, 1.10, 1.19, 1.29 and 1.40 THz. The open circles and the open triangles represent n_e and n_o, respectively. The dash lines are the average index, $(2 \cdot n_o + n_e)/3$ at temperatures below T_c.

In order to describe the real refractive indices of e-ray (n_e), o-ray (n_o) and $(2 \cdot n_o + n_e)/3$ varied with different frequencies, Fig. 4.7 depicts the temperature-dependent data at three frequencies (0.34 THz, 0.70 THz, 0.98 THz) respectively. As Fig. 4.7 shown, n_e, n_o and average refractive indices decrease with increasing frequency.

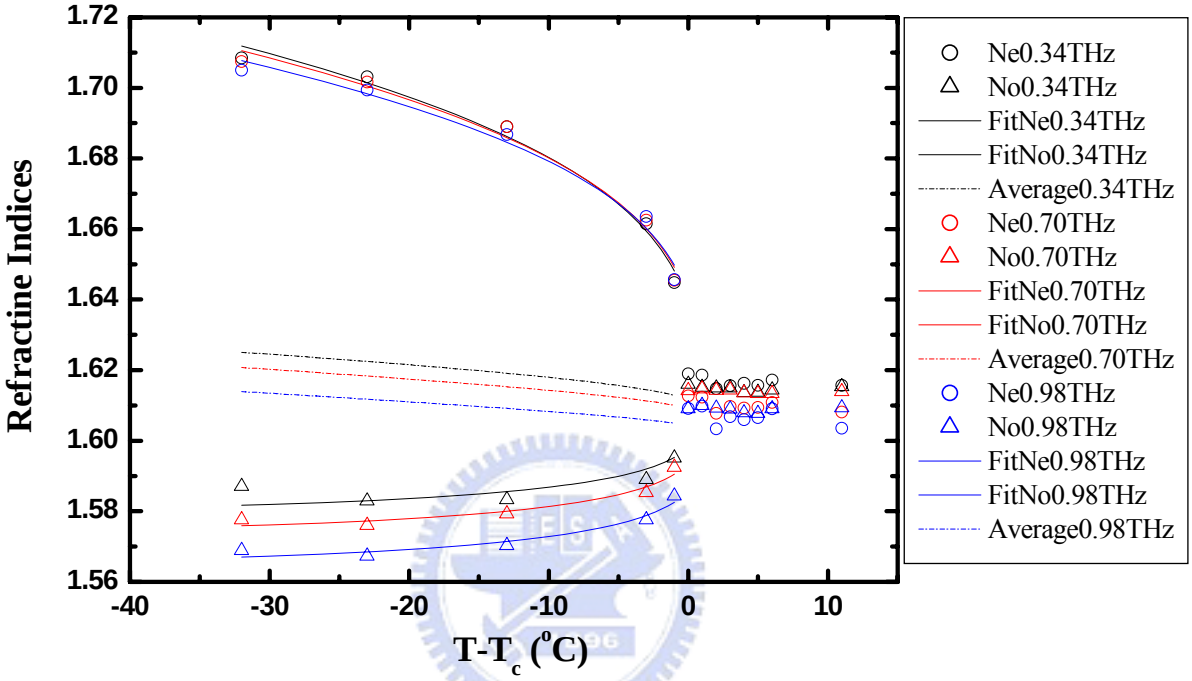

Fig. 4.7 Extraodinary and ordinary refractive indices of E7 are plotted as functions of reduced temperature at frequency of 0.34 (Black), 0.70 (Red) and 0.98 (Blue) THz. The open circles and the open triangles represent n_e and n_o, respectively. The dash lines are the average index, $(2 \cdot n_o + n_e)/3$ at temperatures below T_c.

4.2-2 Temperature Effect on $<n^2>$ and $<n>$

In order to validate the part of results of **Table. 4.1**, we plot the average refractive index $<n>$ of temperature dependence and fit the data by Eq. (3.31) for 0.34, 0.41, 0.53, 0.70, 0.80, 0.89, 0.98, 1.10, 1.19, 1.29, 1.39 THz. Results are shown as **Fig. 4.8 (a)** and **(b)**. Here, the open circles represent the experimental data and the solid lines are the results of fitting.

$$<n(T)>= A - BT \tag{3.31}$$

We also list the fitting parameters A and B in **Table. 4.2**. In comparison of **Table. 4.1,** the fitting parameter A is almost the same, and the order of the fitting parameter B is approximately 10^{-4}.

Table. 4.2 The fitting parameters of Eq. (3.31) for frequencies from 0.34 to 1.40THz.

THz	A	B(K^{-1})
0.34	1.7787	5.05×10^{-4}
0.41	1.7804	5.03×10^{-4}
0.53	1.7505	4.15×10^{-4}
0.70	1.7235	3.42×10^{-4}
0.80	1.7165	3.24×10^{-4}
0.89	1.7010	2.90×10^{-4}
0.98	1.7006	2.89×10^{-4}
1.10	1.6945	2.78×10^{-4}
1.19	1.6743	2.16×10^{-4}
1.29	1.6674	1.90×10^{-4}
1.40	1.6974	2.96×10^{-4}

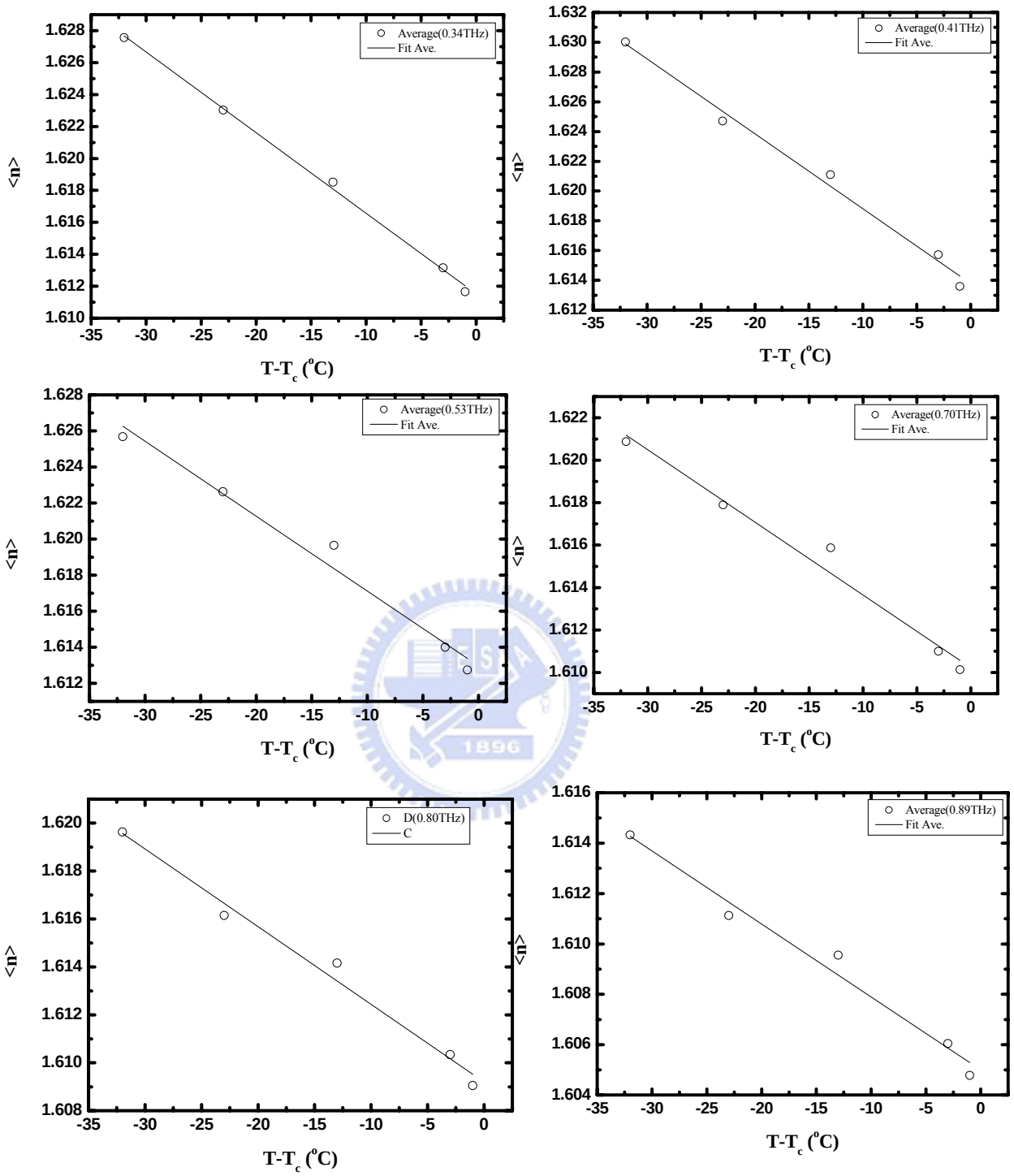

Fig. 4.8 (a) Average refractive indices of E7 are plotted as functions of reduced temperature at frequency of 0.34, 0.41, 0.53, 0.70, 0.80 and 0.90 THz. The open circles represent the experimental data and the solid lines are the results of fitting.

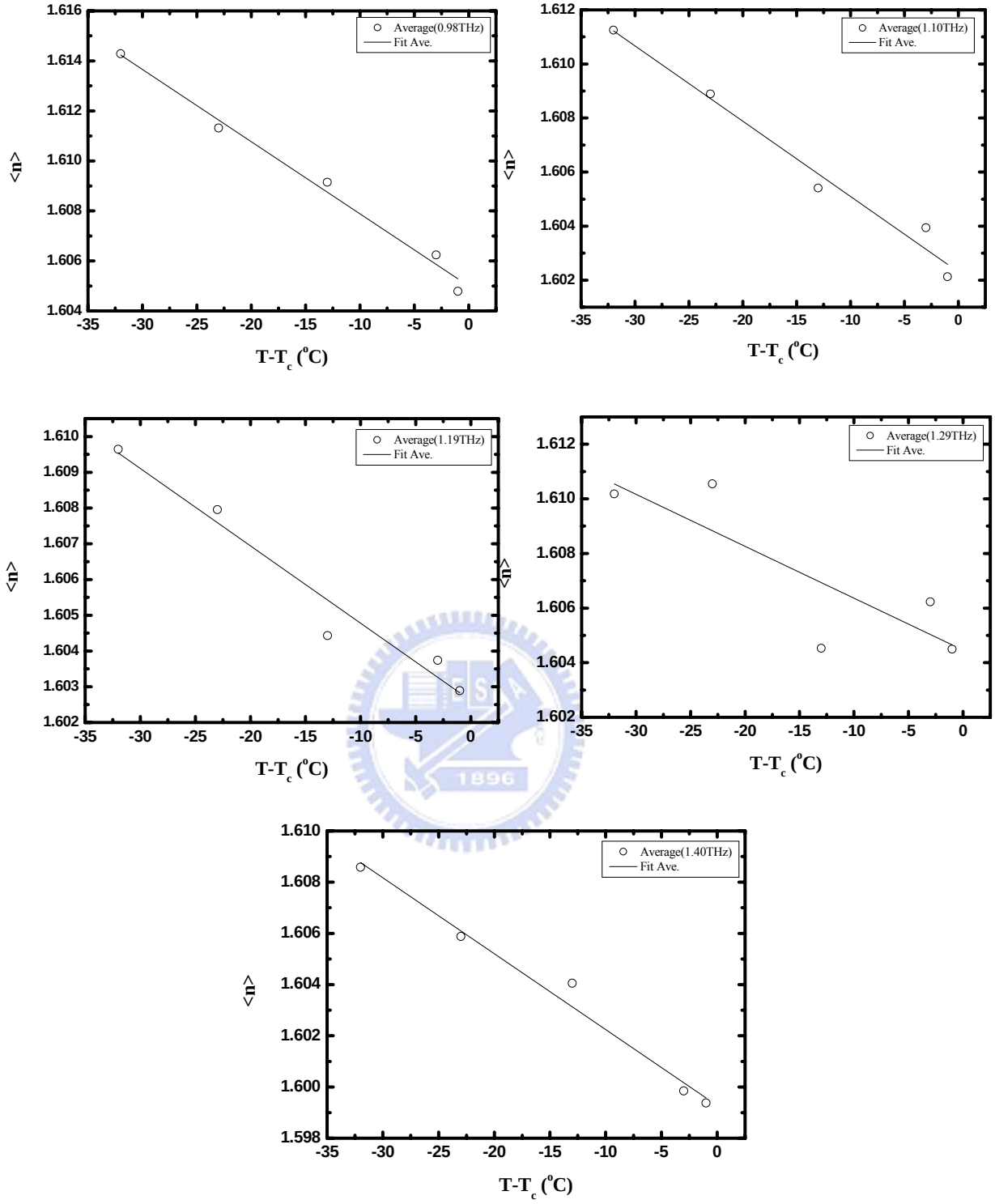

Fig. 4.8 (b) Average refractive indices of E7 are plotted as functions of reduced temperature at frequency of 0.98, 1.10, 1.19, 1.29 and 1.40 THz. The open circles represent the experimental data and the solid lines are the results of fitting.

In order to describe the average refractive indices varied with different frequencies, Fig. 4.9 depicts the temperature-dependent data at four frequencies (0.70 THz, 0.89 THz, 1.10 THz, 1.40THz) respectively. As Fig. 4.9 shown, average refractive indices decrease linearly with increasing frequency.

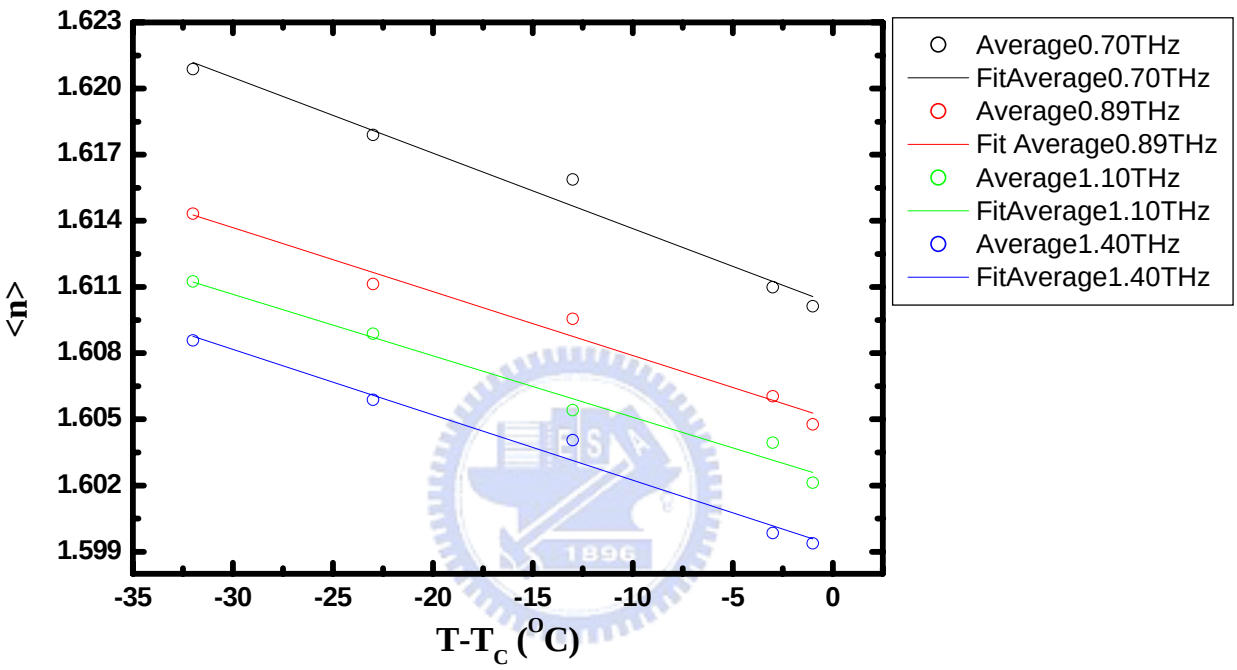

Fig. 4.9 Average refractive indices of E7 are plotted as functions of reduced temperature at frequency of 0.70 (**Black**), 0.89 (**Red**), 1.10 (**Green**), and 1.40 (**Blue**) THz. The open circles represent the experimental data and the solid lines are the results of fitting.

Substituting **Eq. (3.21)** and **Eq. (3.22)** into **Eq. (3.20)**, we can derive as **Eq. (4.1)**:

$$<n^2>=\frac{n_e^2+2n_o^2}{3}=\frac{1+\frac{4\pi N\alpha_e}{1-\frac{4}{3}\pi N<\alpha>}+2+\frac{8\pi N\alpha_e}{1-\frac{4}{3}\pi N<\alpha>}}{3}=\frac{3+\frac{12\pi N<\alpha>}{1-\frac{4}{3}\pi N<\alpha>}}{3}=1+\frac{4\pi}{1-\frac{4}{3}\pi} \tag{4.1}$$

From the **Eq. (3.27)** and **Eq. (3.34)**, we can derive a relationship between $<n^2>$ and $<n>$ [**62**]:

$$\frac{<n>}{<n^2>+2}\approx\frac{\frac{3\sqrt{2}}{4}+\frac{\sqrt{2}\pi}{1-\frac{4}{3}\pi}}{3+\frac{4\pi}{1-\frac{4}{3}\pi}}=\frac{\sqrt{2}}{4} \tag{4.2}$$

After rearranging **Eq. (4.2)**, we can derive:

$$<n^2>\approx 2\sqrt{2}<n>-2\approx(2\sqrt{2}A-2)-2\sqrt{2}BT \tag{4.3}$$

Here, we define $C=2\sqrt{2}A-2$, $D=2\sqrt{2}B$ and **Eq. (4.4)**

$$<n^2(T)>\approx C-DT \tag{4.4}$$

Eq. (4.4) depicts that $<n^2>$ decreases linearly when the temperature increases. This phenomenon is the same as temperature dependent $<n>$, but $<n^2>$ decreases faster than $<n>$. **Fig. 4.10 (a)** and **(b)** is shown the temperature-dependent $<n^2>$, and the fitting parameters (C, D) are also listed in **Table. 4.3**.

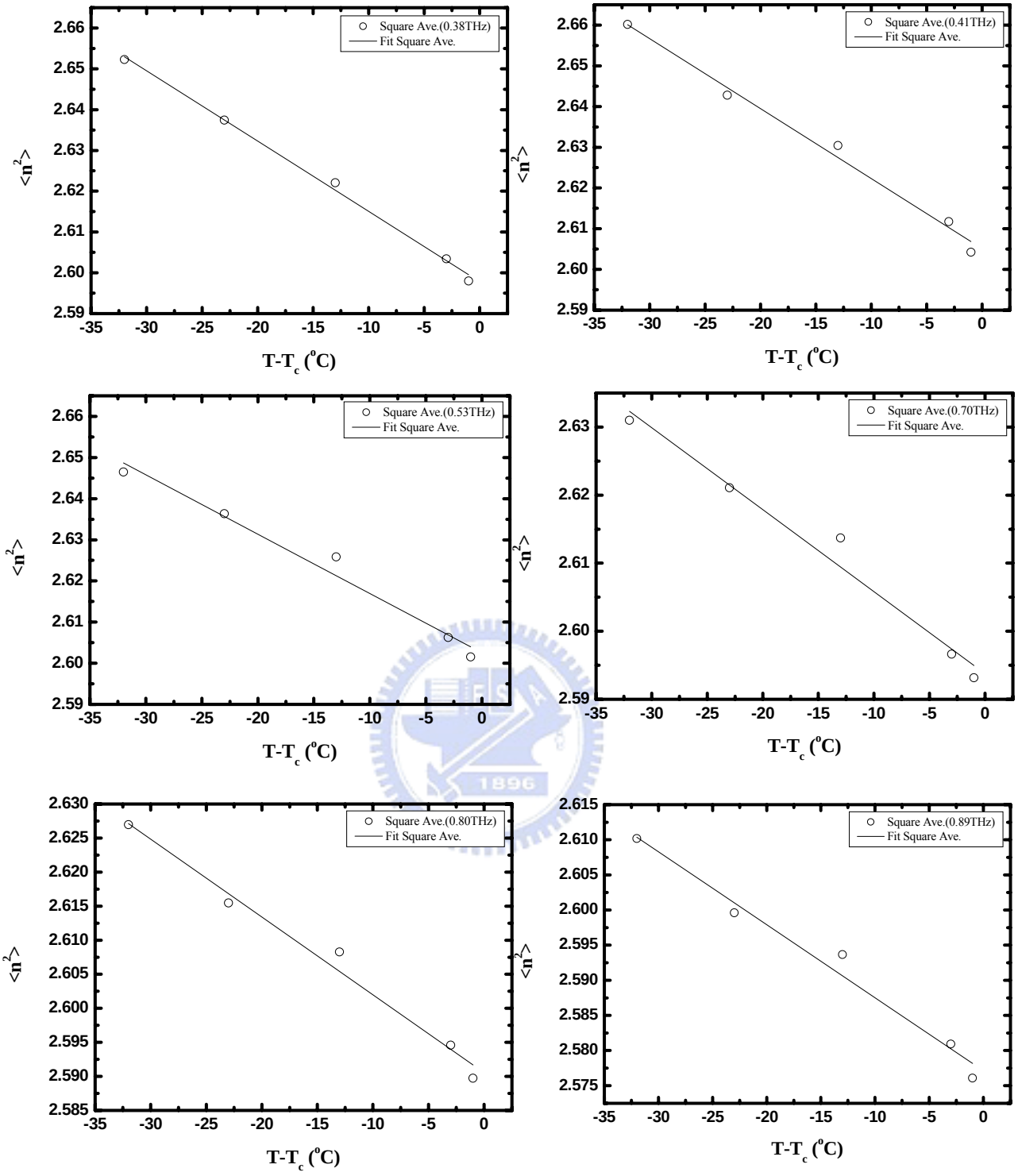

Fig. 4.10 (a) $< n^2 >$ of E7 are plotted as functions of reduced temperature at frequency of 0.34, 0.41, 0.53, 0.70, 0.80 and 0.90 THz. The open circles represent the experimental data and the solid lines are the results of fitting.

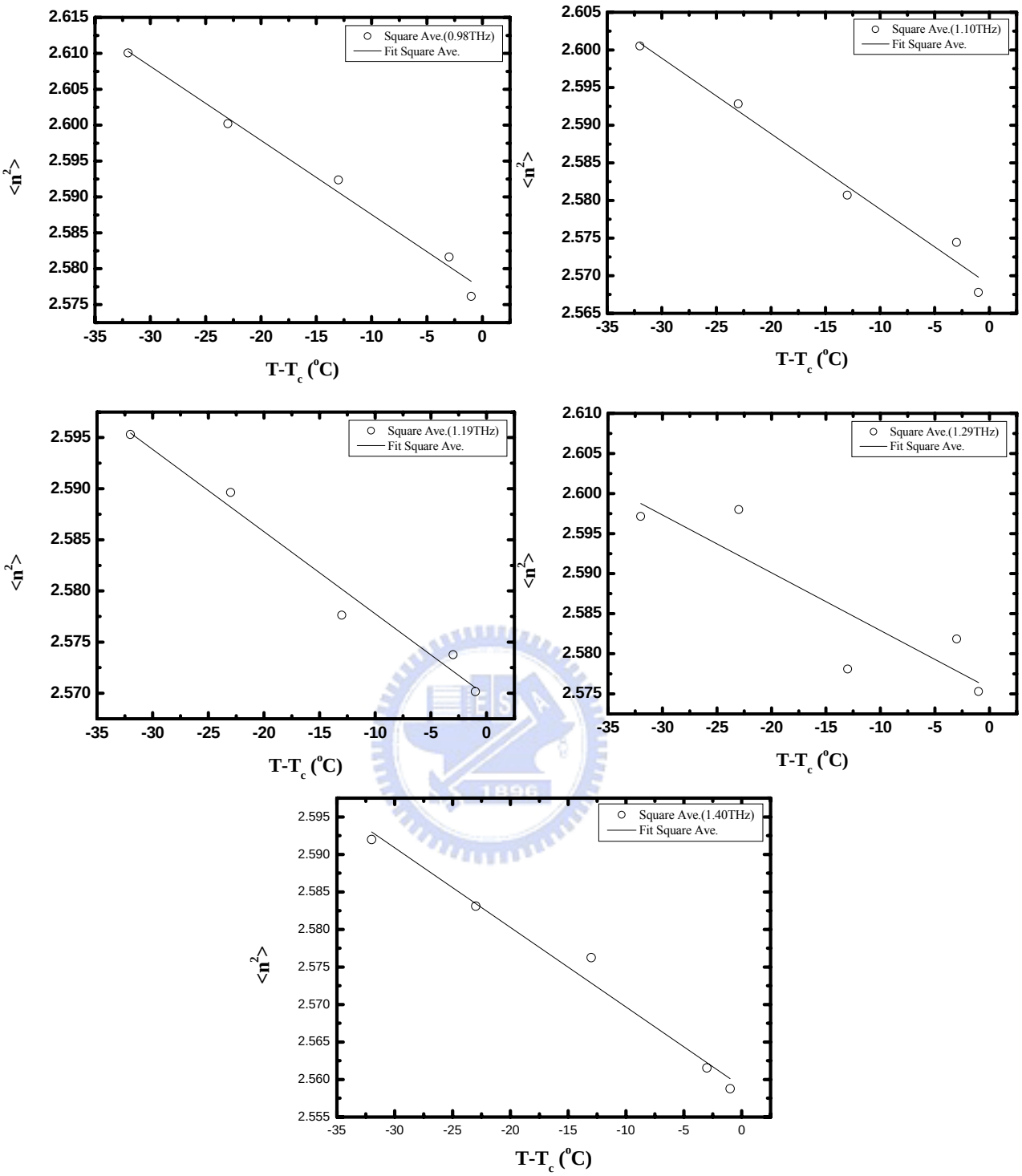

Fig. 4.10 (b) $<n^2>$ of E7 are plotted as functions of reduced temperature at frequency of 0.98, 1.10, 1.19, 1.29 and 1.40 THz. The open circles represent the experimental data and the solid lines are the results of fitting.

THz	C	D(K^{-1})
0.34	3.1684	1.72×10^{-3}
0.41	3.1736	1.72×10^{-3}
0.53	3.0796	1.44×10^{-3}
0.70	2.9927	1.21×10^{-3}
0.80	2.9691	1.14×10^{-3}
0.89	2.9211	1.04×10^{-3}
0.98	2.9190	1.03×10^{-3}
1.10	2.9009	1.00×10^{-3}
1.19	2.8357	0.80×10^{-3}
1.29	2.8143	0.72×10^{-3}
1.39	2.9103	1.06×10^{-3}

Table. 4.3 The fitting parameters of Eq. (3.37) for frequencies from 0.34 to 1.40THz.

In order to describe $<n^2>$ varied with different frequencies, Fig. 4.11 depicts the temperature-dependent data at four frequencies (0.70 THz, 0.89 THz, 1.10 THz, 1.40THz) respectively. As Fig. 4.11 shown, $<n^2>$ decreases linearly with increasing frequency.

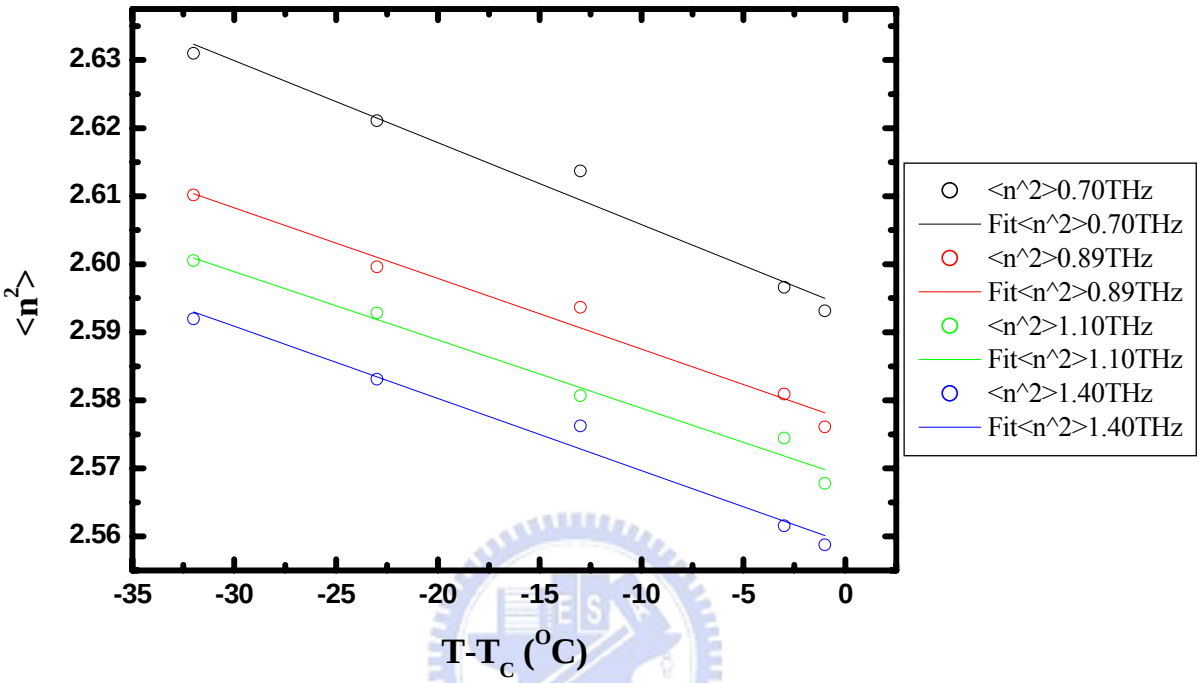

Fig. 4.11 $<n^2>$ of E7 are plotted as functions of reduced temperature at frequency of 0.70 (**Black**), 0.89 (**Red**), 1.10 (**Green**), and 1.40 (**Blue**) THz. The open circles represent the experimental data and the solid lines are the results of fitting.

4.3 Temperature Effect on Birefringence and order parameter

The birefringence of aligned LC is the difference between n_e and n_o, and also relates to the order parameter of LC molecules. Generally, the birefringence of LCs is the function of the temperature, and the relation between birefringence (Δn) and order parameter (S) can be described as **Eq. (3.38)** [**62**]:

$$\Delta n(T) = (\Delta n)_o (1 - T/T_c)^{\beta} = (\Delta n)_o \cdot S \tag{3.38}$$

Here, the parameter β is a material constant which is not too sensitive to the molecular structures of LCs. **Fig. 4.12 (a)** and **(b)** describe the temperature-dependent birefringence of E7, and the fitting parameters $(\Delta n)_0$ and β is also shown as **Table. 4.4**. These fitting parameters are consistent with the **Table. 4.1**, and the parameter β is almost the same with the reference of visible, far infrared and near infrared range [**49**].

THz	$(\Delta n)_0$	β
0.33708	0.2501	0.2903
0.41035	0.2421	0.2826
0.52760	0.2616	0.2941
0.69613	0.2637	0.2902
0.79872	0.2555	0.2766
0.89398	0.2647	0.2725
0.98191	0.2566	0.2598
1.09916	0.2601	0.2483
1.19442	0.2632	0.2554
1.28968	0.2653	0.2543
1.39227	0.2675	0.2588

Table. 4.4 The fitting parameters of Eq. (3.38) for frequencies from 0.34 to 1.40THz.

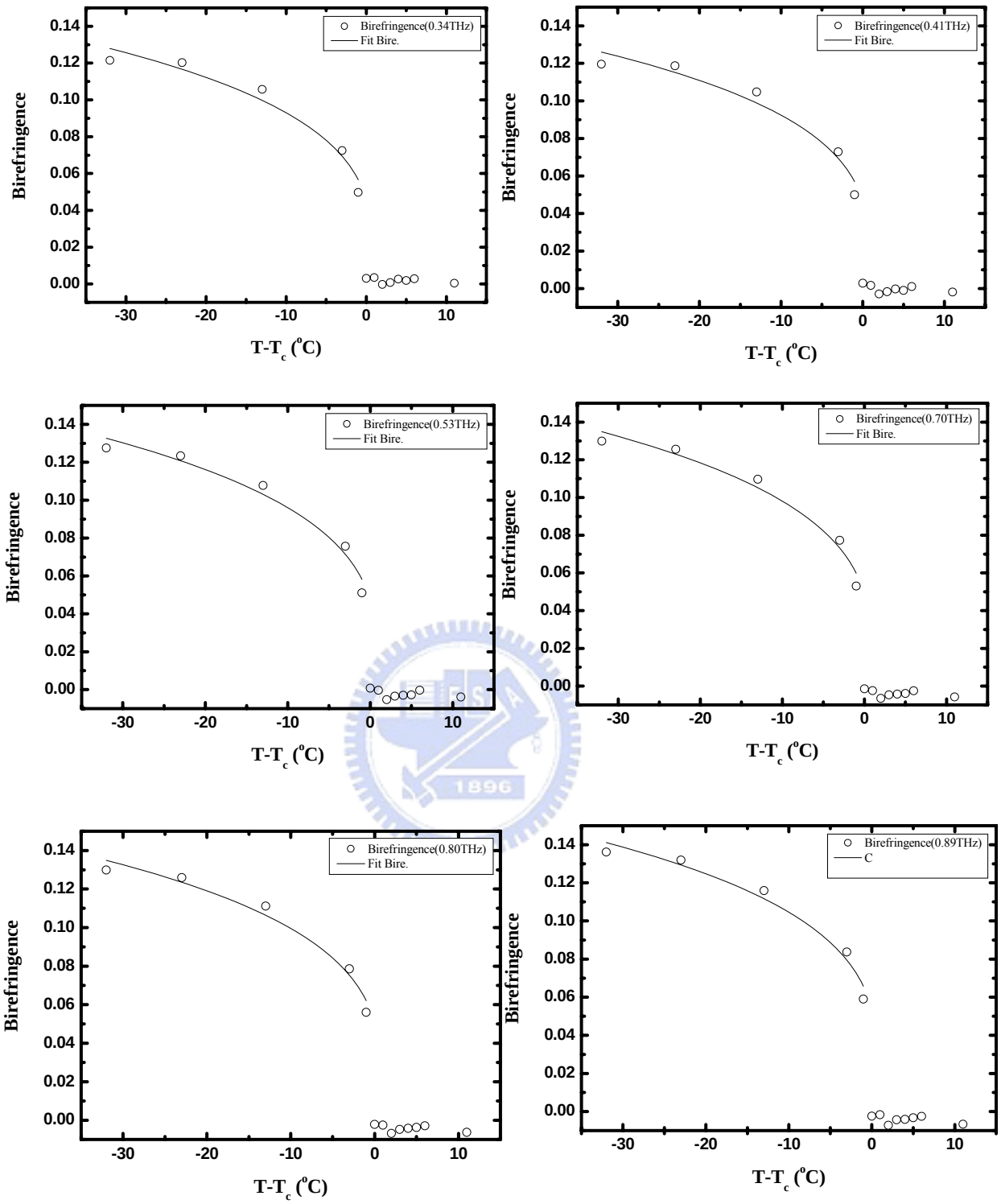

Fig. 4.12 (a) Δn of E7 are plotted as functions of reduced temperature at frequency of 0.34, 0.41, 0.53, 0.70, 0.80 and 0.90 THz. The open circles represent the experimental data and the solid lines are the results of fitting.

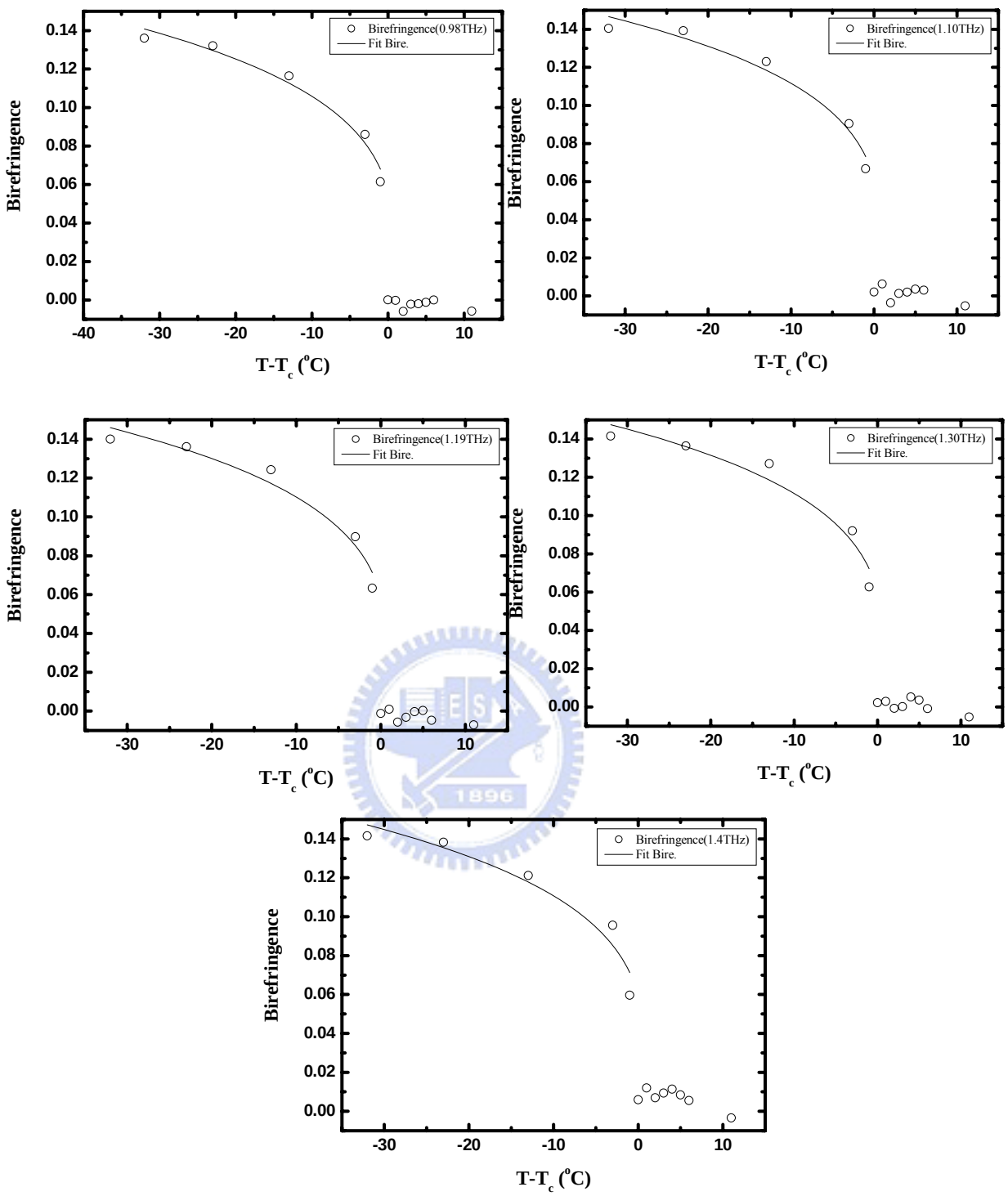

Fig. 4.12 (b) Δn of E7 are plotted as functions of reduced temperature at frequency of 0.98, 1.10, 1.19, 1.30, 1.40 THz. The open circles represent the experimental data and the solid lines are the results of fitting.

In order to describe the birefringence varied with different frequencies, Fig. 4.13 depicts the temperature-dependent data at three frequencies (0.34 THz, 0.80 THz, 1.10 THz) respectively. As Fig. 4.13 shown, birefringence increases with increasing frequency.

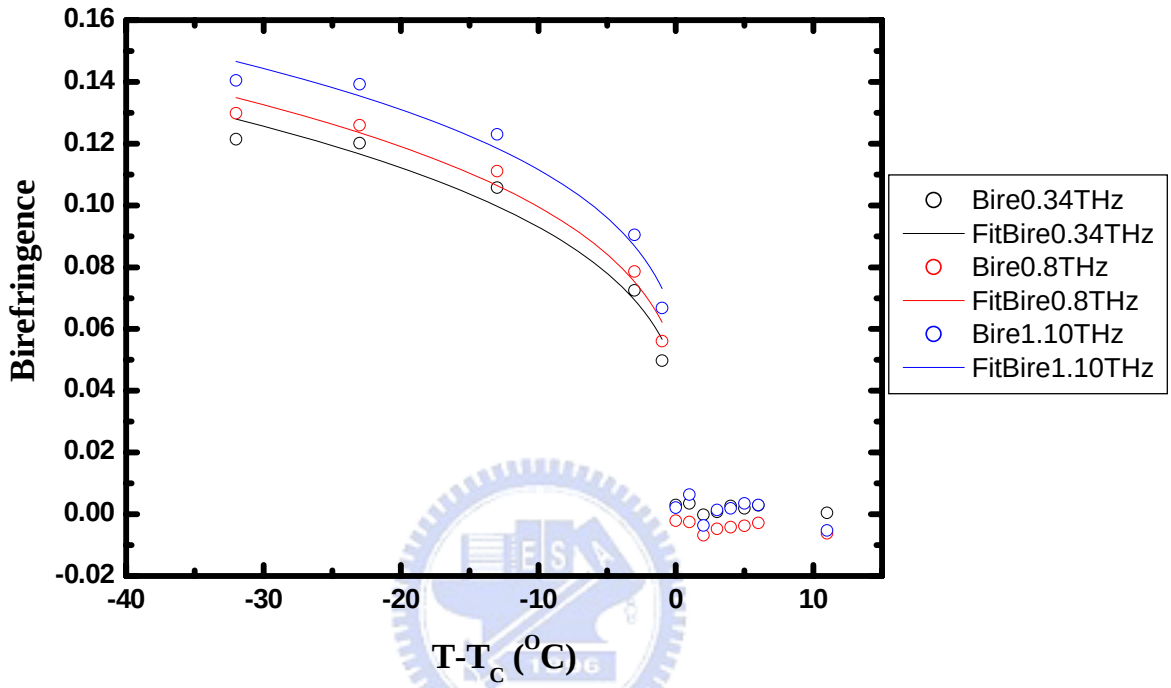

Fig. 4.13 Birefringence of E7 are plotted as functions of reduced temperature at frequency of 0.34 (**Black**), 0.80 (**Red**) and 1.10 (**Blue**) THz. The open circles represent the experimental data and the solid lines are the results of fitting.

On the other hand, the frequency dependence of Δn of E7 at 26°C is shown as **Fig. 4.14**. We find that it always increases with frequency from 0.12 ± 0.01 to 0.14 ± 0.01, and the average of birefringence in the range of 0.2 to 1.4 THz is 0.13 ± 0.01. In comparison with millimeter wave, infrared wave and visible range, we conclude the Δn of the THz range is close to the value of millimeter (Δn = 0.13~0.15) but different from the Δn of visible (Δn = 0.21~0.26) and infrared (Δn = 0.18~0.21) range.

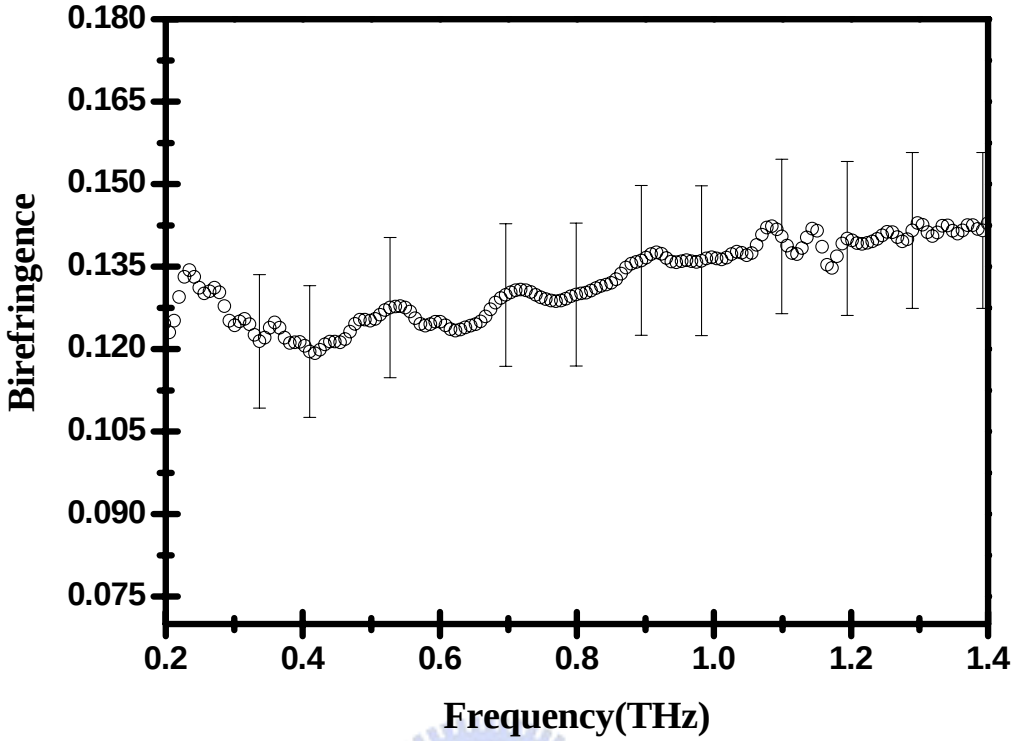

Fig. 4.14 Birefringence of E7 measured at 26°C are plotted as a function of frequency.

4.4 Temperature Dependence of Gradient of Refractive Indices

So far, the temperature gradient of n_e is negative for most of the LC. By the different LC materials and operating temperature, however, the temperature gradient of n_o will change from negative to positive by any possibility.

We can derive the **Eq. (4.5)** and **Eq. (4.6)** by temperature derivatives of **Eq. (3.33)** and **Eq. (3.34)** respectively [**64**].

$$\frac{dn_e}{dT} = -B - \frac{2\beta(\Delta n)_0}{3T_c(1-\frac{T}{T_c})^{1-\beta}} \tag{4.5}$$

$$\frac{dn_o}{dT} = -B + \frac{\beta(\Delta n)_0}{3T_c(1-\frac{T}{T_c})^{1-\beta}} \tag{4.6}$$

Here, we have to check the three parameters (B , β , $(\Delta n)_0$), and all of them can be determined by fitting average refractive indices ($< n >$) and birefringence (Δn). From the **Fig. 4.15**, we find the $\frac{dn_e}{dT}$ for E7 is negative throughout its nematic range because n_e decreases with the temperature increasing in the entire nematic phase. On the other hand, the result of $\frac{dn_o}{dT}$ is shown as **Fig. 4.16**. We can find the E7 exhibits a negative $\frac{dn_o}{dT}$ at room temperature and change into large positive number. In the other words, there is a transition temperature which lets the $\frac{dn_o}{dT} = 0$. Here, the transition temperature is defined as cross-over temperature. We show the results clearly as the **Fig. 4.17**.

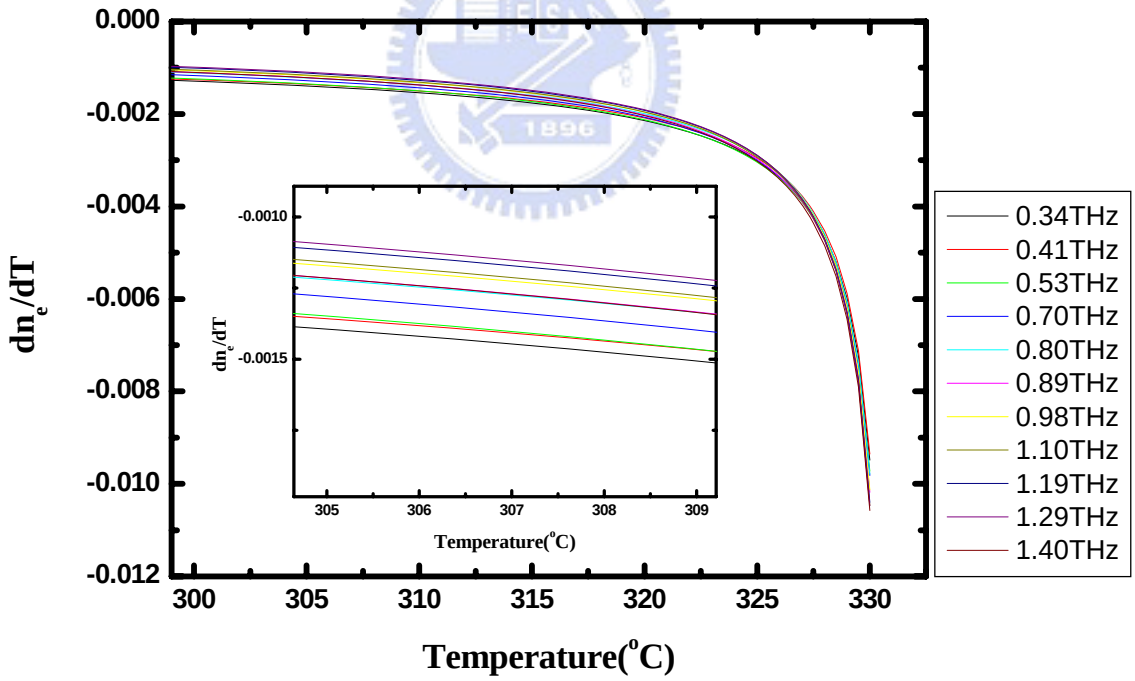

Fig. 4.15 Temperature-dependent $\frac{dn_e}{dT}$ of E7 at different frequencies (0.34, 0.41, 0.53, 0.70, 0.80, 0.89, 0.98, 1.10, 1.19, 1.29 and 1.40 THz), respectively.

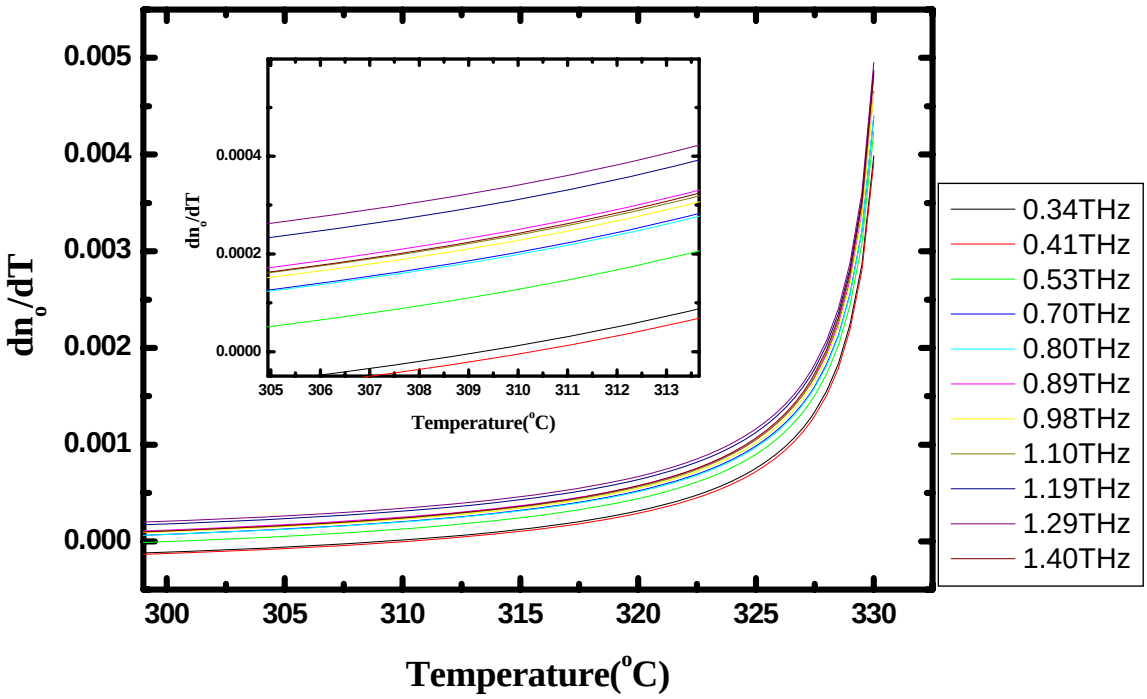

Fig. 4.16Temperature-dependent $\frac{dn_o}{dT}$ of E7 at different frequencies (0.34, 0.41, 0.53, 0.70, 0.80, 0.89, 0.98, 1.10, 1.19, 1.29 and 1.40 THz), respectively.

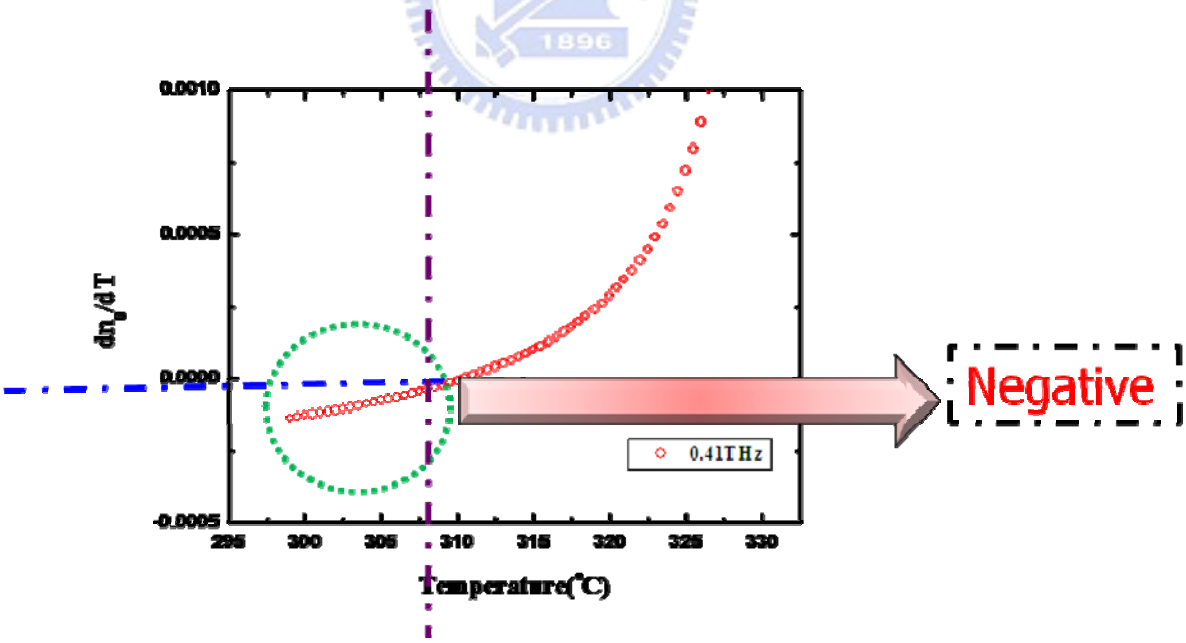

Fig. 4.17 Temperature-dependent $\frac{dn_o}{dT}$ of E7 at 0.41(THz).

Chapter 5 Conclusions

Here, we investigate the optical constants of E7 depending on temperature (26°C ~69°C) and frequency (0.2~1.4THz) in the nematic and isotropic phase, respectively. At 26°C the real parts of indices distribute with $n_e = 1.71 \pm 0.01$, $n_o = 1.57 \pm 0.02$, giving rise to a birefringence of 0.14 ± 0.01 and the index of isotropic phase fall at 1.61 ± 0.01 in the 0.2 to 1.4 THz range. The order parameter extracted from temperature-dependent birefringence of E7 coincides approximately with the results in visible region (589 *nm*). On the other hand, for the imaginary part of the refractive indices, we note that $\kappa_e = 0.014 \pm 0.002$, $\kappa_o = 0.036 \pm 0.004$ and κ in the isotropic phase is 0.030 ± 0.005. Most of all, the extended Cauchy equations describing the temperature dependence of refractive indices of liquid crystal is confirmed completely in this study.

References

1. Ernst Lueder, Liquid Crystal Displays Addressing Schemes and Electro-optical Effect (Wiley, 2001)
2. K. C. Lim, J. D. Margerum and A. M. Lackner, Appl. Phys. Lett. 62 (10) (1993)
3. F. Yang, J. R. Sambles, Appl. Phys. Lett. 79, 3717-3719 (2001)
4. Eric R. Mueller, The Industrial Physicist **27**, Aug./Sept. (2003)
5. Daniel Mittleman, Sensing with Terahertz Radiation, 1st ed. (Spring, New York, 2002)
6. D. Spence, P. Kean and W. Sibbett. Opt. Lett. 16, 42 (1991)
7. M. van Exter, Ch. Fattinger and D. Grischkowsky, Appl. Phys. Lett. 55, 337 (1989)
8. M. van Exter, D. Grischkowsky, IEEE Trans. Microwave Theory Tech. 38, 1684 (1990)
9. X.-C. Zhang, B. Hu, J. Darrow and D. Auston. Appl. Phys. Lett 56, 1011 (1990)
10. Q. Wu, X. –C. Zhang, Appl. Phys. Lett. 68, 1604-1606 (1996)
11. Iam-Choon Khoo, Liquid Crystals Physical Properties and Nonlinear Optical Phenomena (Wiley, 1995)
12. P. G. de Gennes, J. Prost, *The Physics of Liquid Crystals*, **2nd ed.** (Oxford, New York, 1983).
13. Jun Li, Student, Chien-Hui Wen, Sebastian Gauza, Ruibo Lu, and Shin-Tson Wu, J. Display Technol. 1, 51-61 (2005)
14. Eugene Hecht, Optics 3rd ed. (Addison Wesley Longman, New York, 1998)

15. K. C. Lim, J. D. Margerum, A. M. Lackner, Appl. Phys. Lett. 62 (10) (1993)

16. Chao-Yuan Chen, Cho-Fan Hsieh, Yea-Feng Lin, Ru-Pin Pan and Ci-Ling Pan, Opt. Express 12 (12) (2004)

17. C. F. Hsieh, R. P. Pan, T. T. Tang, H. L. Chen and C. L. Pan, Opt. Lett. 31, 1112-1114 (2006)

18. I. H. Libon, S. Baumgä, M. Hempel, N. E. Hecker, J. Feldmann, M. Koch and P. Dawson, Appl. Phys. Lett. 76, 2821-2823 (2000)

19. F. Yang, J. R. Sambles, Appl. Phys. Lett. 79, 3717-3719 (2001)

20. H. Nemec, P. Kuzel, L. Duvillaret, A. Pashkin, M. Dressel and M. T. Sebastian, Opt. Lett. 30, 549-551 (2005)

21. Chao-Yuan Chen, Ci-Ling Pan, Cho-Fan Hsieh, Yea-Feng Lin and Ru-Pin Pan, Appl. Phys. Lett. 88, 101107 (2006)

22. I-Chen Ho, Ci-Ling Pan, Cho-Fan Hsieh and Ru-Pin Pan, Opt. Lett. 33 (2008)

23. Martin van Exter, Ch. Fattinger, and D. Grischkowsky, Optical Letter 14, 20 (1989)

24. A. S. Krishnagopal, V. Kumar, Radiat. Phys. Chem. 70, 559 (2004)

25. H. P. Freund, G. R. Neil, Proceedings of IEEE 87, 782 (1999)

26. R. Kompfner, N. T. Williams, Proc. IRE 41, 1602 (1953)

27. T. Y. Chang, T. J. Bridges, Opt. Commun. 1, 423 (1970)

28. M. Inguscio, G. Moruzzi, K. M. Evenson and D. A. Jennings, J. Appl. Phys. 60, 161 (1986)

29. M. Bass, Phys. Rev. Lett. 9, 446 (1962)

30. A. Bonvalet, Appl. Phys. Lett. 67, 2907 (1995)

31. O. S. Heavens, R. W. Ditchburn, Insight into Optics (1987)

32. Justin T. Darrow, Xi-Cheng Zhang, David H. Austion and Jeffrey D Morse, IEEE J. Quantum electron 28, 1607 (1992)

33. M. J. Lederer, B. Luther-Davies, H. H. Tan, C. Jagadish, M. Haiml, U. Seifner, and U. Keller, Appl. Phys. Let. 74, 1993 (1999)

34. M. Lambsdorff, J. Kuhl, J. Rosenzweig, A. Axmann, and Jo. Schneider, Appl. Phys. Let. 58, 1881 (1991)

35. M. J. Lederer, B. Luther-Davies, H. H. Tan, C. Jagadish, M. Haiml, U. Seifner, and U. Keller, Appl. Phys. Let. 74, 1993 (1999)

36. B. Salem, D. Morris, V. Aimez, J Veerens, J Beauvais and D Houde., J. Phys.: Condens. Matter 17 7327-7333 (2005)

37. M. Mikulics, E. A. Michael, M. Marso, M. Lepsa, A. van der Hart, and H. Lüth, A.Dewald, S. Stančeк and M. Mozolik and P. Kordoš, Appl. Phys. Lett. 89, 071103, (2006)

38. S. Kono, M. Tani and K. Sakai, IEE, Proc. Optoelectron. 149, 105-109 (2002)

39. Sang-Gyu Park, Michael R. Melloch and Andrew M. Weiner, IEEE J. Quantum Electronics. 35, 810-819 (1999)

40. S Kono, Masahiko Tani and Kiyomi Sakai, Appl. Phys. Lett. 79, 898-900 (2001)

41. S. E. Ralph, D. Grischkowsky, Appl. Phys. Lett. 60, 1070 (1992)

42. Q. Wu, X.-C. Zhang, Appl. Phys. Lett. 70, 1784 (1997)

43. Q. Wu, X.-C. Zhang, Appl. Phys. Lett. 71, 1285 (1997)

44. F. G. Sun, G. A. Wagoner and X.-C. Zhang, Appl. Phys. Lett. 67, 1656 (1995)

45. J. Bromage, I.A. Walmsley and C.R.Stroud, Appl. Phys. Lett. 75, 2181 (1999)

46. S. Kono, M. Tani, G. Ping and K. Sakai, Appl. Phys. Lett. 77, 4104 (2000)

47. Tsung-Ta Tang, Ru-Pin Pan, Yi-Chao Wang and Ci-Ling Pan, Ferroelectrics 364, 72-77 (2008)

48. Jun Li, Student, Chien-Hui Wen, Sebastian Gauza, Ruibo Lu, and Shin-Tson Wu, J. Display Technol. 1, 51-61 (2005)

49. Jun Li, Shin-Tson Wu, Stefano Brugioni, Riccardo Meucci, and Sandro Faetti, J. Appl. Phys. 97, 073501 (2005)

50. S. Brugioni, R. Meucci, Infrared Physics & Technology 49, 210–212 (2007)

51. Shin-Tson Wu, Phys. Rev. A 33, 1270-1274 (1986)

52. S. Brugioni, R. Meucci, Infrared Physics & Technology 46, 17–21 (2004)

53. Fuzi Yang, J. R. Sambles, Appl. Phys. Lett. 79 No. 22, 26 (2001)

54. Fuzi Yang, J. R. Sambles, Appl. Phys. Lett. 81, No. 11, 9 (2002)

55. Fuzi Yang, J. R. Sambles, Liq. Cryst. 30, No. 5, 599-602 (2003)

56. M. Koeberle, T. Göbel, D. Schönherr, S. Mueller, R. Jakoby, P. Meissner and H.-L. Hartnagel, German Microwave Conference (2008)

57. H. Mada and S. Kobayashi, Mol. Cryst. Liq. Cryst. 33, 47 (1976)

58. J. D. Jackson, Classical Electrodynamics, 2nd ed. (Wiley, New York, 1962)

59. Kittel, Introduction to Solid State Physics, 7th ed (Wiley)

60. M. F. Vuks, Opt. Spectrosc. 20, 644 (1966)

61. Jun Li ,Shin-Tson Wu, Journal of Applied Physics 96, 6253-6258 (2004)

62. Jun Li, Sebastian Gauza, and Shin-Tson Wu, Journal of Applied Physics 96, 19-24 (2004)

63. A. D. Buckingham, Molecular Electro-optics, (Marcel Dekker, New York, 1976)

64. Jun Li, Sebastian Gauzia, and Shin-Tson Wu, Optics Express 12, 2002-2010 (2004)